1   Word count: 12113

2   **REVISION 2**

3

4   **Hydrologic regulation of clay-mineral transformations in a**

5   **redoximorphic soil of subtropical monsoonal China**

6

7   Lulu Zhao [a], Hanlie Hong [a, *], Qian Fang [a, *], Hetang Hei [b], Thomas J. Algeo [a, c, d]

8

9   [a] *State Key Laboratory of Biogeology and Environmental Geology, Hubei Key*

10   *Laboratory of Critical Zone Evolution, School of Earth Sciences, China University*

11   *of Geosciences, Wuhan 430074, China*

12   [b] *Yunnan Earthquake Agency, Kunming 650224, China*

13   [c] *Department of Geology, University of Cincinnati, Cincinnati, OH 45221-0013, USA*

14   [d] *State Key Laboratory of Geological Processes and Mineral Resources, China*

15   *University of Geosciences, Wuhan 430074, China*

16   Corresponding authors: H. Hong (honghl8311@aliyun.com);

17   Q. Fang (qian.fang@cug.edu.cn)

18

19   **ABSTRACT**

20   Clay-mineral evolution in supergene environments is commonly a complex

21   process subject to hydrologic influences on clay-mineral transformations, yet these

22   influences remain insufficiently investigated to date. A Quaternary red soil profile

23   with evident redoximorphic features in subtropical monsoonal China was investigated

24   with a focus on processes of secondary clay-mineral transformation. Evidence

25   provided by soil physical and chemical descriptions, clay-mineral analysis,

26   spectroscopic characterization, extractions of pedogenic Al and Fe species, and

27   geochemical compositions reveals a complex relationship of clay minerals and iron

28   phases to pedogenic weathering conditions as a function of depth in the study soil

29   profile. The studied profile can be divided into a homogenous horizon (HH; 0-2.0 m),

30   a redoximorphic horizon (RH; 2.0-6.0 m), and a basal layer (BL; 6.0-7.2 m), and these

31   three horizons are dominated by various intermediate clay phases. The HH is

32   characterized by moderately acidic conditions (mean pH = 5.2) and low total organic

33   content (TOC; TOC $\leq$ 2.1 g kg^{-1}). More importantly, compared with the lower horizons,

34   the HH contains significantly more active acid-forming cations, as reflected by a

35   greater abundance of Al phases and higher aluminum saturation levels. We infer that

36   the occurrence of hydroxy-interlayered vermiculite (HIV) in the HH is tightly coupled

37   with the nature of the soil acidic pools, which include both H$^+$ ions (i.e., pH) and active

38   acid-forming cations (e.g., Al^{3+} and Fe^{3+}). The reaction pathway from primary

39   minerals to final weathering products appears to be highly sensitive to dynamic

40   hydrological processes. HIV is favored in generally oxic, well-drained soil systems

41   with adequate acidic cations to maintain acidic weathering. When soils are more

42   waterlogged and the aqueous solution is dominated by base cations, primary minerals

43   tend to transform to smectite group minerals. Therefore, discrete smectite,

44   interstratified illite-smectite (I-S), and interstratified kaolinite-smectite (K-S) were

45   observed only in the RH and BL. We present a novel framework that links

46   clay-mineral transformation pathways to soil hydrological disturbances, providing new

47   insights into understanding the kinetics of water-mineral interactions in natural soil

48   systems.

49

50   **Keywords**: Pedogenesis; chemical weathering; vermiculite; iron oxides; redox

51   reactions; water-rock interaction

52

INTRODUCTION

54   Chemical weathering is one of the key factors that convert bedrock into soils,

55   modifying surficial landforms, regulating the long-term carbon cycle, and modulating

56   the Earth's climate (Kump et al. 2000; Chorover et al. 2007; Jin et al. 2011;

57   Goodfellow et al. 2016). Clay minerals are the most reactive inorganic materials in

58   soils, playing critical roles in many geologic and environmental processes, such as

59   control of the fate of pollutants, uptake and release of bioessential nutrients, and

60   stabilization of soil organic matter (Dong 2012; Andrade et al. 2018; Churchman

61   2018). In supergene weathering zones, primary minerals may transform into other clay

62   species through a sequence of intermediate clay species (e.g., vermiculite, smectite, and

63   their associated interstratified clay minerals; Churchman and Lowe 2012) via diverse

64   pathways prior to the formation of endmember products (Hong et al. 2015; He et al.

65   2017). Understanding the transformation processes and mechanisms involved is of

66   great importance to unraveling the evolution of pedogenic systems in which such

67   alteration occurs (Cuadros et al. 2018; Li et al. 2020).

68   The main pathways of clay-mineral transformation are mediated by the ambient

69   weathering conditions in the soil environment. A single assemblage of primary

70   minerals give rise to different intermediate minerals owing to variation in the

71   conditions of weathering. Weathering generally occurs in water or aqueous solution

72   (Churchman and Lowe 2012; Fang et al. 2019), facilitating chemical reactions such as

73   hydration-hydrolysis, adsorption-desorption, and oxidation-reduction (Essington

74   2015). The hydrologic conditions (including solution pH and chemistry, redox

75   conditions, and water flux) thus play a decisive role in the kinetics, processes, and

76   ultimate products of mineral alteration (Churchman and Lowe 2012). Despite the

77   considerable body of literature on the formation and alteration of clay minerals (e.g.,

78   Wilson 2004; Andrade et al. 2018; Mavris et al. 2018), there is still debate regarding

79   how hydrologic factors control and affect pathways of clay-mineral transformation

80   (Fang et al. 2019; Georgiadis et al. 2020).

81   Quaternary red soils (QRSs) have covered tropical/subtropical areas of southern

82   China (~23 % of China's land surface) since the mid-Pleistocene (He et al. 1983; Hu et

83   al. 2010; Hong et al. 2015). The QRSs are products of syndepositional pedogenesis

84   under a warm and humid climate, widely distributed on river terraces, hills, and alluvial

85   fans (Wilson et al. 2004; Hong et al. 2016; Zhao et al. 2017). The seasonal advance and

86   retreat of the summer monsoon in East Asia produces a distinct alternation of wet and

87   dry seasons, which leads to dynamic hydrologic conditions within the region of QRS

88   formation (Ding and Chan 2005; Kundzewicz et al. 2020). Clay-mineral

89   transformations of the QRSs record environmental changes in southern China during

90   the Quaternary, allowing them to serve as important paleoclimatic archives (Hong et al.

91   2012; Zhao et al. 2017). Previous studies have suggested that typical QRS profiles

92   consist of a single depositional-pedogenetic cycle, corresponding to an upper Xiashu

93   loess horizon (i.e., loess formed since the late Pleistocene on the middle to lower

94   reaches of the Yangtze River, which is often viewed as an extension of the loess of

95   northern China) and an underlying reticulate soil horizon (Hu et al. 2010, 2015; Han et

96   al. 2019). Overall, the Xiashu loess horizon is relatively homogeneous with a yellow to

97   yellow-brown appearance. The reticulate soil horizon contains plinthite, which is

98   defined as a humus-poor, Fe-rich mixture of clay minerals with other minerals,

99   occurring as brown-red redoximorphic masses showing various veining patterns

100   (Bockheim 2014; Hu et al. 2015).

101   Clay mineral assemblages in the QRSs are complex and characterized by various

102   interstratified clay minerals including interstratified kaolinite-smectite (K-S; Hong et al.

103   2012), interstratified illite-vermiculite (I-V; Hong et al. 2014), interstratified

104   illite-smectite-kaolinite (I-S-K; Hong et al. 2015), and interstratified illite-smectite (I-S;

105   Hong et al. 2016). I-V and K-S are commonly present in the middle and lower parts of

106   the QRS profiles (Hong et al. 2012, 2014). Thus, QRSs can serve as a valuable archive

107   of information regarding how soil aqueous conditions modulate the pathways of

108   clay-mineral alteration (Hong et al. 2016).

109   This study characterized the evolution of secondary clay-mineral assemblages in a

110   typical QRS profile in South China. An integrated mineralogical, physico-chemical,

111   spectroscopic, and geochemical dataset was used to diagnose in detail the clay-mineral

112   reactions producing these assemblages, and the environmental conditions promoting

113   their formation. This investigation builds on results from previous QRS studies that

114   showed: 1) clay-mineral composition is complex within QRS profiles; and 2)

115   hydroxy-interlayered vermiculite (HIV) and interstratified clay minerals commonly

116   occur in QRS profiles (e.g., Hong et al. 2012, 2015; Zhao et al. 2017). In the present

117   investigation, we attempt to 1) identify coupling between soil redoximorphic features

118   and clay-mineral assemblages; and 2) advance our understanding of how soil

119   hydrologic conditions regulate the formation and transformation of secondary clay

120   minerals.

121

122   **MATERIALS AND METHODS**

123   **Site descriptions and field sampling**

124   The study area is located inside the Jianghan Plain of Hubei Province, central

125   China (Fig. 1). The Jianghan Plain is an alluvial plain situated no more than 35 m above

126   sea level (m.a.s.l.). It is flat and crisscrossed by numerous rivers (e.g., the Yangtze

127 River and its largest tributary, the Han River) and lakes (Zhou et al. 2013; Gan et al.

128 2014). The Jianghan Plain is surrounded by the Dabie Mountains (500–800 m.a.s.l.) to

129 the northeast, the Daba Mountains (1600–3000 m.a.s.l.) and Wushan (2400 m.a.s.l.) to

130 the west, and the Wuling Mountains (~1000–2500 m.a.s.l.) to the southwest (Fig. 1c).

131 The Jianghan Plain is located in a subtropical monsoonal climate zone that is directly

132 influenced by the East Asian and Indian monsoon systems (Fig. 1a-b). The study area is

133 characterized by highly seasonal variations in temperature, precipitation, and wind

134 direction. The mean annual temperature is 17.5 °C (5.0 °C in winter and 28.8 °C in

135 summer), and the total annual precipitation is about 1450 mm with ~60 % of the rainfall

136 occurring during the period from May to September (Hersbach et al. 2019). The climate

137 is classified as *Cfa* according to the Köppen-Geiger climate classification (Kottek et al.

138 2006). During the summer, the East Asian Summer Monsoon (EASM) and Indian

139 Summer Monsoon (ISM) dominate the climate of the Jianghan Plain, causing advection

140 of warm and humid airmasses from the ocean, contributing to its high agricultural

141 productivity (Deng et al. 2014).

142   In this study, soil samples were collected from the Songzi section in the

143 southwestern region of the Jianghan Plain (Fig. 1c). This section represents a typical

144 QRS that consists of an upper Xiashu loess horizon and the underlying reticulate red

145 soil horizon (Hong et al. 2012, 2014). This section is 7.2 m thick and can be divided

146 into upper (0-2.0 m), middle (2.0-6.0 m), and lower (6.0-7.2 m) intervals based on

147 contrasting texture, mineralogy, structure, and redoximorphic features within these

148   horizons (Fig. 2a; Table 1). The upper and middle intervals of the Songzi section match

149   the upper Xiashu loess and the underlying reticulate horizon of QRSs, respectively. The

150   lower interval of the Songzi section corresponds to the basal layer of QRSs but with a

151   coarser particle size. A detailed description of the study section is given in the *Results*

152   section.

153   A total of 72 soil samples was collected at 10-cm intervals continuously from the

154   base to the top of the study section. Prior to geochemical and spectroscopic analyses,

155   several preparatory treatments were performed to generate sample aliquots with

156   different particle sizes, including the bulk soil (i.e., fresh soil samples dried at 45 °C for

157   48 h), a <2-mm fraction (i.e., a fine-earth fraction consisting of ground bulk soil that

158   passes through a 2-mm sieve), a <74-µm fraction (i.e., a fraction consisting of ground

159   <2-mm fraction that passes through a 74-µm (200-mesh) sieve), and a <2-µm fraction

160   (i.e., a clay fraction that was isolated by repeated suspension of an aliquot of the

161   <74-µm fraction with sodium hexametaphosphate and centrifugation). Prior to

162   processing of the clay fraction, carbonates were removed by addition of 0.05-M acetic

163   acid for ~24 h).

164

165   **X-ray diffraction (XRD)**

166   Clay-mineral species were identified based on XRD analysis of the clay-fraction

167   samples (i.e., oriented specimens on glass slides). Four different treatments were

168   applied to the air-dried (AD) XRD mounts, i.e., ethylene glycol solvation (EG),

169   K-saturation at room temperature (K25), and K-saturation with heating to 350 °C

170   (K350) and 550 °C (K550) for 2h. The K saturation was performed on powders

171   recycled /scraped off from the AD mounts. The K saturation was performed twice on

172   each sample using 0.5-M KCl at room temperature, with each saturation interval lasting

173   ~12 h; after the saturation step, excess salt was removed using distilled water to which

174   two drops of 0.5-M KCl were added. The XRD spectra of the K-saturated samples (at

175   room temperature and after heat treatments) were obtained for the same aliquots as used

176   in the AD and EG treatments. For clay-fraction samples of the HH, two additional

177   heating treatments were performed on the K-saturated mounts: K-saturation with

178   heating to 100 °C (K100) and K-saturation with heating to 200 °C (K200), both for 2h,

179   to better test for the presence of HIV. In addition, bulk-sample XRD analysis was

180   performed on the <74-µm fraction using a side-loading method. All XRD

181   measurements were performed using a PANalytical X'pert PRODY2198

182   diffractometer (Netherlands) with Cu-Kα radiation (40 kV, 40 mA). The XRD spectra

183   were recorded from 3 to 65° 2θ at a rate of 4° 2θ/min and a resolution of 0.02° 2θ.

184   The PANalytical HighScore software was used to fit experimental XRD profiles

185   of *00l* reflections over the 3.5-15° 2θ range. The Voigt function was applied to fit the

186   peaks of the EG spectra. Prior to peak fitting, the background of each XRD spectrum

187   was subtracted using a cubic spline method with an automated threshold of 5 sigma

188   using the Jade software. Various combinations of peaks were tested to find the one

189   yielding the minimum residual signal. A series of parameters, including the position of

190   the 001 peak, intensity (i.e., peak height), and half-height width, were used in the

191   calculation. These peak parameters were refined by the least-squares method until they

192   optimally matched the XRD signal. The peak areas were then used as an

193   approximation of the relative abundances of the various clay-mineral phases in the

194   sample. Finally, the amount of each phase was determined by normalizing the sum of

195   the relative abundances to 100%. Because clay minerals are highly complex and have

196   a series of interstratified phases, the results of such curve-fitting techniques are only

197   semiquantitative and used to support or complement other data.

198

199   **Selective extraction**

200   Selective extraction techniques were applied to the <74-μm fraction using sodium

201   pyrophosphate (PP), acid ammonium oxalate (AO), and citrate-dithionite (DC) (Parfitt

202   and Childs 1988). About 0.1 g of powder for each analyzed sample was mixed with 0.1

203   M pyrophosphate (pH = 10) and agitated to extract Al- and Fe-oxyhydroxides bound in

204   organo-metal complexes (i.e., Al_p and Fe_p). The contents of total free Fe and Al (i.e.,

205   Fe_d and Al_d), including all crystalline and amorphous forms in the sample, were

206   determined by extraction with 0.1 M Na-dithionite + 0.3 M Na-citrate (DC extraction;

207   Parfitt and Childs 1988; Rasmussen et al. 2010). The AO method (using 0.1 M

208   ammonium oxalate as an extractant) permitted extraction of poorly crystalline and

209   amorphous Al- and Fe-oxyhydroxides or of so-called short-range-ordered (SRO) iron

210   and aluminum phases (i.e., Al_o and Fe_o) (Shang and Zelazny 2008). The extracted

211   solution was filtered using a 0.2-μm cellulose acetate filter, and concentrations were

212   measured with an Agilent 7500a inductively coupled plasma-mass spectrometer

213   (ICP-MS). The measured concentration data were then used to calculate the contents of

214   different forms of Fe and Al solids. The SRO fractions of Fe- and Al-bearing minerals

215   were assessed using Fe_o/Fe_d and Al_o/Al_d ratios, respectively (Blume and Schwertmann

216   1969; Hall et al. 2018). The contents of secondary crystalline Fe and Al compounds

217   were estimated as $Fe_d - Fe_o$ and $Al_d - Al_o$, respectively (Blume and Schwertmann 1969;

218   Hall et al. 2018).

219

220   **Soil physico-chemical characterization**

221   The fine-earth fraction samples were used for soil physico-chemical

222   measurements. Soil acidity (pH) and redox potential (Eh) were measured in distilled

223   water using a pH/Eh electrode (ORP-501, INESA, China) immersed in a 1:2.5 soil:

224   water suspension after 1 h of stirring with a glass rod. Total organic carbon (TOC) and

225   total nitrogen (TN) contents were analyzed using an Elementar Vario Macro Cube C/N

226   analyzer (Germany). Prior to TOC and TN analyses, each sample was decarbonated

227   using 0.05 mol L^{-1} HCl and washed with distilled water to remove residual acid.

228   The particle-size analysis was conducted using an American Microtrac S3500

229   laser particle sizer with a diameter range of 0.02–2000 μm. The resulting diffraction

230   spectra were transformed to grain-size data using Mie theory (Konert and

231   Vandenberghe 1997). The data were finally output as clay fraction (<2 μm), silt fraction

232   (2-50 μm), and sand fraction (50-2000 μm) in volumetric form with a precision of

233   ±1 %.

234   Exchangeable cations were extracted by 1 mol L^{-1} ammonium acetate (NH$_4$OAc)

235   at pH 7 for Ca^{2+}, Mg^{2+}, K$^+$, Na$^+$ and by 1 mol L^{-1} KCl for Al^{3+} (Madeira et al. 2003;

236   Pincus et al. 2017). The solution was sonicated in order to disaggregate the clay and

237   then let stand for 16 h. The sample was centrifuged until all clay was separated from the

238   supernatant, which was collected for inductively coupled plasma optical emission

239   spectrometry (ICP-OES) analysis using an ICPE-9000 instrument (Shimadzu). The

240   results allowed calculation of the cation exchange capacity (CEC), which was

241   determined as Ca^{2+} + Mg^{2+} + K$^+$ + Na$^+$ + Al^{3+}.

242

243   **Diffuse reflectance infrared Fourier transform (DRIFT) spectroscopy**

244   DRIFT spectroscopy was used to improve the assessment of the evolution of

245   depth-dependent solid phases and mineral crystallinity (Nguyen et al. 1991; Yuan et

246   al., 2004). The DRIFT method is sensitive to poorly crystalline minerals and their

247   complexation with organic matter (Chorover et al. 2004). DRIFT spectra were

248   recorded from 4000 to 400 cm^{-1} using a Nicolet 560 Magna IR spectrometer at 4 cm^{-1}

249   resolution. DRIFT analysis was performed on four sample aliquots: the untreated

250   <74-μm fraction, the <74-μm fraction after AO extraction, the <74-μm fraction after

251   DC extraction, and the clay fraction. Through comparison of differences in DRIFT

252   spectra between the AO-extracted and untreated samples, we evaluated the influence

253   of the AO extraction on soil composition. Through comparison of differences in

254   DRIFT spectra between the DC-extracted and untreated samples, we evaluated the

255   influence of the DC extraction on soil composition. Organic matter was not removed

256   from these samples as it may be closely associated with soil metal(oxy)hydroxides.

257   Each sample was mixed with KBr (1 % by mass) prior to the DRIFT measurement.

258

259   **Elemental geochemistry analyses and weathering proxies**

260   Major-element concentrations were determined by X-ray fluorescence (XRF)

261   spectrometry with a Shimadzu XRF-1800 sequential spectrometer (Japan). Analytical

262   precision was better than 1 %, and the detection limit was ~0.01 wt%. Trace elements

263   and rare earth elements (REEs) were measured by Agilent 7500a ICP-MS with an

264   analytical precision of < 4 % for REEs and 4-10 % for other trace elements. The

265   <74-µm fraction samples were used for the XRF and ICP-MS measurements. The

266   detailed sample digesting procedure for ICP-MS analyses was as follows: (1) 50 mg

267   sample powder was accurately weighed and placed in a Teflon bomb; (2) 1ml HNO_3

268   and 1ml HF were slowly added into the Teflon bomb; (3) Teflon bomb was put in a

269   stainless steel pressure jacket and heated to 190°C in an oven for >24 hours; (4) After

270   cooling, the Teflon bomb was evaporated to incipient dryness and then 1ml HNO_3 was

271   added and evaporated to dryness again; (5) 1ml HNO_3, 1ml MQ water, and 1 ml

272   internal standard solution of 1 ppm In were added, and the Teflon bomb was resealed

273   and placed in the oven at 190°C for >12 hours; (6) The final solution was transferred to

274   a polyethylene bottle and diluted to 100 g by the addition of 2 % HNO_3.

275   The most commonly used weathering proxy, chemical index of alteration (CIA),

276   was calculated using the measured elemental data. CIA was calculated as

277    $[Al_2O_3/(CaO^* + Na_2O + K_2O + Al_2O_3)] \times 100$ (molar ratio), where CaO* represents the

278   amount of CaO in the silicate fraction of the sample (Nesbitt and Young 1982). The

279   degree of chemical weathering was also evaluated using the M^+-4Si-R^{2+} system (i.e.,

280   weathering alteration scale-WIS), which was proposed by Meunier et al. (2013). The

281   M^+, 4Si, and R^{2+} parameters are the recalculated values of atomic proportions, where

282   M^+ corresponds to $Na^+ + K^+ + 2Ca^{2+}$, R^{2+} denotes $Mg^{2+} + Fe^{2+} + Mn^{2+}$, and 4Si

283   represents number of Si^{4+} cations divided by 4. The parameter Δ4Si is calculated as

284    $[(4Si_{soil} - 4Si_{UCC}) \times 100]/(100 - 4Si_{UCC}) \times 100$, where the subscripts "soil" and "UCC"

285   represent the Si concentrations in the bulk soil sample and upper continental crust

286   (UCC), respectively (McLennan 2001). Higher Δ4Si denotes a higher intensity of

287   chemical weathering, and the maximum weathering intensity of weathering is reached

288   when the parent rock is completely weathered to kaolinite (i.e., Δ4Si = 100) (see

289   Meunier et al. 2013, for details).

290   REE concentrations were normalized to upper continental crust (UCC)

291   (McLennan 2001) prior to further calculations. The Ce anomaly (Ce/Ce*), which can

292   track soil-redox status (Laveuf and Cornu 2009), was calculated as (Compton et al.

293   2003):

294        $$\frac{Ce}{Ce*} = \frac{(Ce_{soil}/Ce_{UCC})}{[(La_{soil}/La_{UCC})^{0.5}(Pr_{soil}/Pr_{UCC})^{0.5}]} \qquad (1)$$

295   where the subscripts "soil" and "UCC" represent the REE concentrations in the bulk

296   soil sample and UCC, respectively. Values < 1 and > 1 represent "negative" and

297   "positive" Ce anomalies, respectively.

298

299   **Thermogravimetric (TG) analysis**

300   TG analysis was performed on a Netzsch STA409PC thermal instrument. The

301   measurement was carried out by heating the sample from 30 to 1000 °C in steps of

302   10 °C min^{-1} under a nitrogen flow of 60 mL/min. About 10 mg of each clay fraction

303   sample were heated in a corundum crucible. The derivative thermal gravimetric (DTG)

304   curve was derived from the TG curve.

305

306   **Statistical analyses**

307   To determine whether differences in extraction Al/Fe and soil iron mineralogy

308   between various soil horizons are significant, we performed one-way analysis of

309   variance (ANOVA). Differences were considered significant at a 99% (3σ) confidence

310   level.

311

312   **RESULTS**

313   **Morphological description and physicochemical compositions**

314   The Songzi soil is classified as a Plinthaquult (Ultisol) according to the US Soil

315   Taxonomy (Soil Survey Staff 2010), with a loam to silty clay texture (Table 1). The

316   study section has a diagnostic argillic subsurface horizon with typical redoximorphic

317   features in its lower part (Fig. 2). The middle interval (2.0-6.0 m) displays prominent

318   redoximorphic features (Fig. 2b). The Songzi section can be divided into a surface

319   homogeneous horizon (HH; 0-2.0 m), a middle redoximorphic horizon (RH; 2.0-6.0 m),

320   and a basal layer (BL; 6.0-7.2 m). Several sub-horizons can be identified within each

321   horizon (Table 1). The redoximorphic features in the RH consist mainly of

322   yellow-reddish matrix accompanied by black Mn-enriched concentrations (i.e.,

323   coatings; Soil Survey Staff 2010), red Fe-enriched earthy materials (i.e., plinthites;

324   Weil and Brady 2017), and white veins/mottles (Fig. 2b). The coatings are generally

325   distributed along microfissures or fill micropores, with diameters less than a centimeter

326   (Fig. 2b). The plinthites have a redder Munsell hue (2.5YR 4/8) than the surrounding

327   soil matrix (5YR 8/6), range in size from 2 to 5 cm, and are commonly surrounded by

328   veins. The veins are generally less than 10 cm long and randomly oriented.

329   The soil solution in the entire study section varies from acidic (in the HH) to

330   circumneutral (in the BL), with pH values ranging from 4.8 to 6.5 (Table 2). The redox

331   potential of the Songzi section decreases with depth, from >400 mV in the HH to <300

332   mV in the BL. The soil has low contents of TOC (0.7–2.1 g kg^{-1}) and TN (0.3–0.7 g

333   kg^{-1}), with the highest values occurring near the top of the section. Most soil samples

334   have high silt content (56.5-72.9 %; mean 63.3 %), intermediate clay content

335   (23.5-41.2 %; mean 33.7 %), and low sand content (0.3-5.2 %; mean 2.7 %). The

336   highest clay contents are found in the upper part of the RH (2.4-4.5 m).

337   CEC ranges from 24.4 to 39.8 mmol kg^{-1} with exchangeable sites dominantly

338   occupied by Ca and Mg. CEC is positively correlated with total clay content ($r = +0.75$,

339     $p < 0.001$, $n = 17$) and reaches a maximum value in the upper part of the RH. The

340   relative proportion of Al in the exchangeable sites (i.e., Al$_{ex}$/CEC), which is closely

341   related to the presence of Al polymers in the interlayers of expandable clay minerals

342   (Jin et al. 2010; Graham et al. 1989), is low compared with Ca, Na, Mg, and K. The

343   highest contribution of Al to total CEC occurs in the upper HH (Al$_{ex}$/CEC = 7.63 % at

344   0.3 m), while its contribution is negligible in the RH and BL.

345

346   **XRD analysis**

347   The clay fractions of the HH, RH, and BL (using various treatments) exhibit

348   similar XRD characteristics throughout the Songzi section (Figs. 3 and S1). The main

349   non-clay phases are quartz (~4.3 and 3.3 Å), feldspar (two weak peaks around 3.2 Å),

350   and small amounts of goethite (~4.2 Å), hematite (~2.7 Å), and gibbsite (~4.4 and 4.8

351   Å) (Figs. 3 and S2). The diffraction peaks for Fe/Al-(oxy)hydroxides are somewhat

352   more evident in the RH and BL.

353   Illite and kaolinite are the dominant phases in the clay fraction (Figs. 3 and S1).

354   The main differences in soil clay mineralogy between soil horizons are associated with

355   2:1 clay minerals yielding reflections at ~14 Å (Figs. 3 and S1). The intensity and

356   position of the ~14-Å peak changed after the EG treatment and heat treatment of the

357   K-saturated mounts at various temperatures, which offer a basis for identification of the

358   2:1 clay minerals. The XRD spectra of slowly heated, K-saturated mounts are deemed

359   the most useful in recognizing the presence of HIV (Barnhisel and Bertsch 1989). In

360   samples from the HH, the ~14-Å peak gradually shifted to ~12-12.6 Å in the K100 and

361   K200 spectra and then disappeared at higher temperatures (Fig. 3a-d). Peak residues at

362   10.2-11.5 Å after K550 treatment are found in the HH samples, although these peaks

363   are weak in some samples (Fig. 3a-d). The prominent peak at ~10 Å after K550

364   treatment is primarily from illite, with only a minor contribution from collapse of the

365   ~14-Å peak. According to Meunier (2007), hydroxy-interlayered smectite (HIS) does

366   not expand fully after EG treatment but only to ~15 Å and then collapses to ~12 Å after

367   K saturation. Thus, the occurrence of HIS in the Songzi samples can be discounted.

368   These considerations provide solid evidence for the presence of a hydroxy-interlayered

369   form of vermiculite with a relatively low degree of Al-polymerization in the HH

370   (Barnhisel and Bertsch 1989; Moore and Reynolds 1997; Korchagin et al. 2019). The

371   presence of HIV is also supported by DRIFT and exchangeable Al data (see the sections

372   *DRIFT analysis* and *Crystalline forms of Fe and Al*). HIV was not observed in samples

373   from the RH and BL (Fig. 3e, f). The K550 spectrum indicates that all samples contain

374   kaolinite, since the 7.1-Å peak is no longer present (Fig. 3).

375   The ~14-Å peak in the HH samples show scarcely any expandable character after

376   the EG treatment, suggesting the absence of swelling clay minerals (i.e., smectite or

377   vermiculite) in the HH (Figs. 3 and S1). Considering the results above, the ~14-Å peak

378   in the HH samples is primarily attributable to HIV. In a few samples from the lower HH

379 (e.g., sample at 1.2 m), the ~14-Å peak partially collapsed to ~10 Å after the K25

380 treatment (Fig. 3c), possibly indicating the presence of high-charge interlayers in HIV

381 (Barnhisel and Bertsch 1989; Meunier 2007). The peak at ~14 Å is particularly weak in

382 the RH, indicating a very minor occurrence of HIV, smectite, or vermiculite. The ~14-Å

383 peak in the BL samples expanded to ~17.5 Å after the EG treatment (Figs. 3d and S1),

384 suggesting the presence of smectite in the BL. We are not able to exclude the presence

385 of low-charge vermiculite in the BL as the potential expanded vermiculite peak at ~16

386 Å is weak and may overlap with that of expanded interstratified illite-smectite (I-S)

387 (Figs. 3 and S1).

388   Consistent with the general distribution of smectite, interstratified I-S and

389 kaolinite-smectite (K-S) are present mainly in the BL. There is a notable "platform"

390 between ~10.6 Å and ~12 Å in the BL samples, which splits into two peaks after EG

391 treatment, a rightward peak at ~9.1-9.6 Å and a leftward peak at ~11.5-13.6 Å. This

392 observation provides solid evidence for the presence of I-S in the BL. For samples

393 containing I-S with a relatively high proportion of smectite layers, the leftward peak

394 may even shift to >15 Å (Cuadros and Altaner 1998). As noted above, it is difficult to

395 discriminate this potential peak from the peak of EG-expanded smectite. However, this

396 discrimination is unnecessary for the focus of the present study. K-S can be more

397 readily identified: there is a broad and asymmetrical peak at ~7.1-7.9 Å with a

398 pronounced tail in the low-angle region in most AD mounts from the lower RH and BL,

399 which often shows expandable character in the corresponding EG mounts, i.e., the peak

400   shape is marked by a leftward shift or becomes slightly expanded (Figs. 3 and S1). We

401   cannot exclude the presence of halloysite in these samples, although that mineral does

402   not respond to EG treatment, making K-S a more likely contributor to the tail in the

403   low-angle region (Figs. 3 and S1; Righi et al. 1999; Dudek et al. 2007). However, the

404   difference in the ~7.1-7.9 Å region between the AD and EG treatments is not obvious in

405   some samples from the lower RH and BL, suggesting the absence of K-S.

406   Peak decomposition and fitting of XRD spectra were performed on the basis of

407   the aforementioned clay-mineral identifications (Fig. 4), and the fitted curves are

408   generally consistent with experimental XRD spectra. The peak decomposition and

409   fitting procedure yields semiquantitative mineral compositions, which clearly reveal

410   differences in clay-mineral assemblages over a range of soil depths (Fig. 4). For

411   example, our results show that HIV is preferentially enriched in the upper HH, and

412   that smectite is preferentially enriched in the lower BL (Fig. 4). These results are

413   consistent with clay-mineral identifications based on saturation and heating

414   experiments (Moore and Reynolds 1997).

415

416   **DRIFT analysis**

417   The DRIFT spectra of the untreated <74-μm fractions, the <74-μm fractions after

418   AO extraction and DC extraction, and the clay fractions in the HH (0.3 m) and RH

419   (5.1 m) are shown in Figure 5a. The assignments of inorganic bands are listed in Table

420   3. The <74-μm fractions have strong absorption bands for quartz and clay minerals,

421   consistent with the result from bulk-sample XRD analysis (Fig. S2). The persistence

422   of clay minerals after the AO extraction attests to the slower kinetics of dissolution of

423   these clay phases relative to the amorphous phases (Chorover et al. 2004). The broad

424   intense band in the 3500–3000 cm^{-1} range represents the stretching vibrations of

425   H-bonded hydroxyl (O-H) groups of alcohols, phenols, and water molecules

426   (Ellerbrock et al. 1999), and this band decreases after the AO extraction and collapses

427   after the DC extraction. Three prominent bands in the region of 2000-1700 cm^{-1} are

428   caused by weak overtones/combination bands of quartz (Nguyen et al. 1991). The

429   doublet at 800 cm^{-1} and 780 cm^{-1} and the sharp band at 697 cm^{-1} also correspond to

430   quartz. These bands were absent in the clay-fraction samples, and the remaining bands

431   at 754 cm^{-1} and 697 cm^{-1} are indicative of kaolinite and illite, respectively. It is

432   worthy to note that the bands for mineral features may be overlapped with organic

433   substances. For example, OH stretching region may be influenced by hydroxyls groups

434   found in the organic matter. The aromatic C=C stretching and HOH deformation band

435   of adsorbed water at 1640 cm^{-1} and aliphatic C–H bending band at 1405 cm^{-1} are

436   evident in the clay-fraction samples (Baes and Bloom 1989). Organic bands below

437   1200 cm^{-1} (i.e., angular deformations of aromatic compounds at ~430, 470, 540, 697,

438   and 915 cm^{-1}, and C-O stretching of hydrophilic compounds at ~1025 and 1100 cm^{-1};

439   Aguiar et al. 2013; Nuzzo et al. 2020) are generally masked by intense quartz and

440   phyllosilicate bands.

441   Variations in clay-mineral assemblages are strongly reflected in the O-H

442   stretching region (3900–2900 cm^{-1}; Fig. 5b). The bands at 3699 cm^{-1} and 3650 cm^{-1}

443   are characteristic of the Al-OH vibration in the octahedral sheet of kaolinite

444   (Madejová 2003; Mavris et al. 2018). These two bands become sharper and more

445   pronounced at greater depths within the study section, indicating more kaolinite in the

446   RH and BL relative to the HH. The band at 3625 cm^{-1} represents inner hydroxyl

447   groups between the tetrahedral and octahedral sheets of kaolinite and 2:1 dioctahedral

448   phases (Zhang et al. 2016). In the BL, the greater intensity of the band at 3699 cm^{-1}

449   relative to that at 3625 cm^{-1} may be correlated with enhanced kaolinization of

450   interstratified K-S (Cuadros and Dedek 2006). The apparent band at 3650 cm^{-1} may

451   represent improved crystallinity of the kaolinite structure (Fig. 5b; Cuadros and

452   Dudek 2006). The band at ~3699 cm^{-1} may also be related to occurrence of an

453   Al-hydroxy interlayer in 2:1 clay minerals (i.e., HIV), although it overlaps with the

454   kaolinite band (Barnhisel and Bertsch 1989; Szymański et al. 2014).

455   Comparison between DRIFT spectra of the <74-µm fraction and DC-treated

456   <74-µm fraction can also provide evidence for the presence of HIV in the HH (Fig.

457   5a). The band at 540 cm^{-1} is commonly attributed to Al-OH in the interlayer

458   hydroxide sheet (Barnhisel and Bertsch 1989), which became notably weaker

459   (compared to the nearby band at 470 cm^{-1}) after the DC extraction for the HH samples.

460   However, the reduction in intensity of the 540-cm^{-1} band is not observed for samples

461   from other horizons. Considering that the DC extraction can dissolve Al-OH in the

462   interlayer hydroxide sheet of HIV (Barnhisel and Bertsch 1989), we suggest that the

463   comparison of the DRIFT spectra confirms the presence of HIV in the HH samples,

464   consistent with the XRD analysis.

465

466   **Crystalline forms of Fe and Al**

467   Differences in Fe and Al dissolution by the three primary extraction methods (PP,

468   AO, and DC) reflect variable proportions of the crystalline forms of Fe and Al

469   throughout the section (Fig. 6; Table S1). The contents of these Fe and Al phases

470   generally follow the orders $Fe_d > Fe_o > Fe_p$ and $Al_d > Al_o > Al_p$, respectively. There is no

471   significant difference in concentrations of Fe_p and Al_p between the HH and RH-BL ($p =$

472   0.21 and 2.97 for Fe_p and Al_p, respectively; Fig. 6a). Contents of amorphous or

473   short-range-order (SRO) minerals plus organically bounded Fe and Al phases are low

474   throughout the Songzi section: Fe_o and Al_o range from 1.01 to 2.82 g kg^{-1} and 0.48 to

475   1.03 g kg^{-1}, respectively. The HH contains significantly more Fe_o and Al_o (mean = 2.58

476   and 0.95 g kg^{-1}, respectively) than the RH and BL (means = 1.78 and 0.75 g kg^{-1},

477   respectively) (F > 7, $p < 0.01$; Table S1). The contents of total extractable Fe and Al are

478   notably different in the various horizons (F = 12.64 and 7.22 for Fe_d and Al_d,

479   respectively; $p < 0.01$), with significantly higher contents of extractable Fe and Al in

480   the RH-BL (mean Fe_d = 14.51 g kg^{-1}; mean Al_d = 1.59 g kg^{-1}) compared to the HH

481   (mean Fe_d = 12.22 g kg^{-1}; Al_d = 1.46 g kg^{-1}) (Fig. 6c; Table S1). Total Fe and Al

482   concentrations do not show significant differences between the HH and RH-BL ($p =$

483   0.28 and 1.54 for Fe_t and Al_t, respectively; Fig. 6d).

484   Fe_o/Fe_d represents the SRO fraction of Fe-bearing minerals in soils, and Fe_d–Fe_o

485   represents the crystalline pedogenic Fe pool (Blume and Schwertmann 1969; Coward

486   et al. 2017; Hall et al. 2018). Similarly, Al_o/Al_d and Al_d–Al_o represent the SRO fraction

487   of Al-bearing minerals and the crystalline pedogenic Al pool, respectively (Araki and

488   Kyuma 1986; Rennert 2019). Fe_o accounts for only a small fraction of the total Fe pool,

489   as indicated by low Fe_o/Fe_d ratios, which range from 0.07 to 0.26 (Fig. 6e). Amorphous

490   Al phases plus organically bound Al (Al_o), on the other hand, are major components of

491   the total Al pool in the HH, as indicated by high Al_o/Al_d ratios with a mean of 0.66. The

492   SRO fraction of Al-bearing minerals is significantly lower in the RH-BL (F = 9.6, $p <$

493   0.01; Fig. 6e), with a mean Al_o/Al_d ratio of 0.47. The RH and BL contain significant

494   amounts of Fe and Al trapped in crystalline phases, as reflected in elevated Fe_d–Fe_o and

495   Al_d–Al_o values (F > 9, $p < 0.01$; Fig. 6f).

496

497   **Chemical weathering intensity**

498   The geochemical compositions of the bulk soils in the HH, RH, and BL are given

499   in Table 4. The bulk soils generally have a similar, Si-rich chemical composition ($SiO_2 >$

500   67 %). There are, however, some minor differences in chemical composition between

501   soil horizons, especially with regard to the contents of MgO (lower in the BL), CaO

502   (slightly higher in the RH and BL), and alkali metals (lower Na_2O and K_2O in the BL).

503   CIA ranges from 81 to 85, with a mean of 83.5, suggesting an intense weathering

504   condition. The study samples plot close to the 4Si endmember in an M^+-4Si-R^{2+} ternary

505   diagram (Fig. 7), implying major losses of alkaline and alkaline-earth cations (e.g., Na^+,

506   K^+, Ca^{2+}, and Mg^{2+}) and intense chemical weathering (Meunier et al. 2013). The BL

507   samples plot closer to the 4Si endmember than the HH-RH samples, reflecting greater

508   kaolin and Al/Fe-(hydr)oxide content and more intense chemical weathering (Meunier

509   et al. 2013).

510

511   **Trace element and rare earth element geochemistry**

512   Similar to the major element data, trace element concentrations also vary within

513   relatively narrow ranges (Table S2). The distribution patterns of the trace elements are

514   similar for all samples: the Sc, V, Zn, Ga, and Rb contents are close to UCC; Y, Zr, Nb,

515   Cs, Hf, Ta, Th, and U are enriched; and Sr, Sn and Ba are depleted relative to UCC

516   (Fig. S3a). The chondrite-normalized REE patterns of the Songzi samples are

517   presented in Fig. S3b. REE distributions show highly similar features, including

518   enrichment of light-REEs, negative Eu anomalies, and relatively flat heavy-REE

519   distributions. Similar REE distributions have also been reported from the loess

520   profiles in northern and central China (Gallet et al. 1996; Fang et al. 2017). The Songzi

521   samples show positive Ce anomalies in the HH (mean Ce/Ce* = 1.18) and slightly

522   negative Ce anomalies in the BL (mean Ce/Ce* = 0.91) (Fig. 8).

523

524   **Thermogravimetric analysis**

525   Representative TG/DTG curves are shown in Figure S4. The mass loss at ~100 °C

526   corresponds to loss of moisture and evaporation of absorbed water from the interlayers

527   of 2:1 clay minerals (Ma et al. 2015). Mass loss in the 150-200 °C range is generally

528   caused by dehydration of water molecules that are strongly bounded in hydration shells

529   of cations with high hydration enthalpy (e.g., Ca^{2+} and Mg^{2+}). The small peak at

530   ~270 °C in both the HH and RH samples is attributed to dehydration of goethite

531   (Ndzana et al. 2018), which is consistent with XRD results showing a small amount of

532   goethite throughout the Songzi section. A minor mass loss at ~370 °C in the DTG

533   curve can be observed only in the HH samples (Fig. S4a). Mass losses in the range of

534   350-800 °C generally represent dehydroxylation (i.e., release of structural OH groups)

535   of the layer structure in clay minerals.

536

537   **DISCUSSION**

538   **Coupling between soil acidity pools and HIV formation**

539   HIV is found in the upper part of the Songzi section (especially the upper HH)

540   with diminishing content with depth, and this phase completely disappears in the

541   RH-BL (Fig. 8). The presence of HIV in the HH samples has been confirmed by XRD

542   and DRIFT analyses (Figs. 3 and 5). Notably higher exchangeable Al:CEC ratios (i.e.,

543   Al_{ex}/CEC) may also suggest the polymerization of Al in interlayers of vermiculite in

544   the HH (Barnhisel and Bertsch 1989; Jin et al. 2010). Thermal analysis has been used

545   to confirm the presence of hydroxy-interlayered minerals when they are the dominant

546   phases in the soil (Barnhisel and Rich 1963; Barnhisel and Bertsch 1989). Mass loss

547   at 370 °C in the DTG curve, which has been attributed to hydroxy interlayers

548   (Barnhisel and Bertsch 1989), can be observed only in the HH samples (Fig. S4). As

549   such, thermal analysis provides additional evidence for the occurrence of

550   hydroxy-interlayered minerals (HIMs) in the HH. HIMs have also been found to be

551   preferentially enriched in the surface horizons of sediment-derived soils from

552   subtropical Brazil (Andrade et al. 2019). Relative to the Songzi soil, the Brazilian

553   soils developed in a similar climatic background and have similar organic contents but

554   lower pH. Andrade et al. (2019) ascribed the formation of HIMs to high rates of Al

555   release during pedogenic weathering under acidic soil conditions, which influenced

556   the interlayering of Al-polymers in the clay minerals. Interlayering is a common

557   phenomenon in pedogenic 2:1 clay minerals, in which the interlayer materials include

558   cations, hydrated cations, organic molecules, and hydroxide groups or sheets

559   (Meunier 2007; Dietel et al. 2019a, 2019b; Georgiadis et al. 2020). According to Rich

560   (1968) and Meunier (2007), HIV is a fast-forming and unstable phase representing a

561   moderately acidic and oxidizing condition that is often linked to frequent wet-dry

562   cycles. The decisive factor that induces HIV formation in the soil environment,

563   however, remains controversial.

564   Soil acidity pools, which include not only H^+ ions (i.e., pH) but also active

565   acid-forming cations such as aluminum and iron, play an important role in soil

566   chemistry (Weil and Brady 2017). We hypothesize that soil acidity pools controlled

567   formation of HIV in the study profile. Under acidic conditions, H^+ attacks the

568   structure of silicate minerals and promotes the release of Al^{3+} (Sposito 2008). Free

569   Al^{3+} has a strong tendency to hydrolyze, splitting water molecules into H^+ and OH^-

570   ions (Fig. 9b; Weil and Brady 2017), and Al^{3+} combines with OH^- to form

571   hydroxy-aluminum ions $[Al(OH)_x^{y+}]$ (i.e., $AlOH^{2+}$ and $Al(OH)_2^{+}$), from which large

572   Al polymers in the interlayer of 2:1 clay minerals are generated (Meunier 2007; Weil

573   and Brady 2017). During the hydrolysis process, the formation of hydroxy-aluminum

574   ions $[Al(OH)_x^{y+}]$ leaves H^+ in the soil solution, yielding lower pH. Each Al^{3+} ion

575   releases three H^+ ions, making it a strong acid-forming cation (or 'acid cation'). Fe^{3+}

576   has similar properties to Al^{3+} in that it can release H^+ ions during the hydrolysis

577   process. Nevertheless, Fe^{3+} hydrolyzes at extremely low pH conditions (pH < 3),

578   which are not common in natural soils (Weil and Brady 2017; Ying et al. 2020). In

579   soils pH > 3, free Fe^{3+} ions tend to quickly precipitate as iron hydroxides or

580   oxyhydroxides. The hydroxy-iron ions (i.e., $FeOH^{2+}$ and $Fe(OH)_2^{+}$)) tend not to

581   survive long in natural soil systems, which may account for the observation that

582   hydroxy-Fe interlayers are much less common in clay minerals than hydroxy-Al

583   interlayers. The pH of the Songzi soils ranges from 4.8 to 6.5 (Table 2), so we confine

584   our discussion to Al^{3+} (Fig. 9).

585   In the study section, the HH provided an optimal environment for formation of

586   HIV, key features of which included abundant pre-existing 2:1 clay minerals (illite >

587   30 %; Fig. 4; Table S3), low organic matter content (TOC ≤ 2.1 g kg^{-1}), moderately

588   acidic conditions (mean pH = 5.2; Table 2), and a monsoonal climate with oscillating

589   wet and dry cycles. These features are generally consistent with the optimal

590   conditions (e.g., pH ranging from 4.6 to 5.8, low organic matter content, and frequent

591   wet-dry cycles) for formation of HIV proposed by Rich (1968). More importantly, the

592   HH contains a greater quantity of active acid-forming cations than the RH and BL, as

593   reflected in significantly greater amounts of SRO Al- and Fe-oxy(hydr)oxides (mean

594   Al_o and Fe_o = 2.58 and 0.95 g kg^{-1}, respectively) and a higher aluminum saturation

595   percentage (mean Al_{ex}/CEC = 2.9 %) (Fig. 6; Table 2). In the HH, the relatively high

596   concentration of Al_{ex} to CEC reflects the inferred hydrolysis and polymerization of Al

597   in the interlayers of vermiculite in acidic soils (Jin et al., 2010), which is consistent with

598   our XRD and DRIFT results. Compared to the underlying horizons, the HH contains

599   significantly larger amounts of active Al phases, as indicated by its Al_o/Al_d

600   distribution (Figs. 6e and 8g). Al-(hydr)oxides with larger SRO Al fractions (poorer

601   crystallinity) are more readily mobilized than more crystalline phases, leading to

602   greater quantities of free Al^{3+} ions in soil water (Rennert 2019). The HH experienced

603   intense hydrolysis during the deposition–pedogenesis process, and the detrital clay

604   minerals transformed to thermodynamically more stable clay species through

605   chemical weathering (Singer 1980; Huang et al. 2018). The acid ions (especially H^+

606   and Al^{3+}), along with other cations (i.e., Ca^{2+} and Mg^{2+}), accumulated in the HH

607   during the strong hydrolysis process. The adsorption strength of common cations on

608   most clays and humus decreases in the order: $Al^{3+} > Ca^{2+} > Mg^{2+} > K^+ > Na^+$

609   (Evangelou and Phillips 2005). Weathering of illite leads to opening of its interlayers

610 and leaching of K, which can then be substituted by other cations, potentially

611 transforming illite to vermiculite. With adequate acid-cation supply, aluminum ions

612 occupy an increasing proportion of the remaining exchange sites, forming Al-polymer

613 islands in the interlayers of vermiculite/HIV. We infer that the presence of sufficient

614 aluminum ions in soil solution may be a key factor in HIV formation (Fig. 9b).

615 Formation of HIV was not favored in the lower part of the Songzi section (i.e.,

616 RH-BL) (Figs. 3 and 8). In those horizons, pH was higher (mean 6.1), resulting in

617 greater precipitation of Al-OH as hydroxide [$Al(OH)_3^0$] rather than being accumulated

618 in the interlayer of clay minerals (Fig. 9c; Carstea et al. 1970; Hsu 1989).

619 Concentrations of exchangeable aluminum are negligible, and effective CEC is

620 mostly saturated with respect to exchangeable non-acid cations (Ca^{2+}, Mg^{2+}, K^+, and

621 Na^+, i.e., the base cations; Table 2). Moreover, the crystallinity of Fe/Al-(hydr)oxides

622 is statistically greater in the RH-BL than in the HH (Fig. 6), which is evidence of a

623 rapid down section decrease in active Al^{3+} and Fe^{3+} ions. More well-crystalline Fe and

624 Al-(hydr)oxides are present in the RH-BL, as indicated by the wet-chemical

625 extraction results (Fig. 6). The RH exhibits evident redoximorphic characteristics (Fig.

626 2b), which formed in an intermittently water-saturated environment with seasonal

627 redox fluctuations. Redox oscillations promote the direct conversion of SRO materials

628 into more crystalline forms (Thompson et al. 2006), leading to rapid precipitation of

629 active Al^{3+} and Fe^{3+} ions as sesquioxides. The intermittently waterlogged conditions

630 and frequent redox cycles of the study soil led to insufficient acidic cations in the soil

631   acidity pool (especially Al^{3+} and Fe^{3+} ions), breaking the transformation pathway from

632   pre-existing 2:1 clay minerals to HIV. Therefore, the intermediate clay phases in the

633   RH-BL are dominated by the smectite group and its associated interstratified minerals

634   (Fig. 8).

635   HIMs are commonly found in seasonally waterlogged paddy soils (Brinkman

636   1970; Mitsuchi 1974; Wakatsuki 1984; Georgiadis et al. 2020), even though the

637   conditions in these soils are not 'optimal' for formation of HIMs (Rich 1968). Paddy

638   soils are periodically flooded soils characterized by alternately reducing and oxidizing

639   conditions, usually in response to agronomic activity (Weil and Brady 2017). These

640   conditions can induce the decomposition of clay-mineral structures and formation of

641   HIMs (Kyuma 1978; Georgiadis et al. 2020). For example, Fe^{3+} can be reduced to

642   mobile Fe^{2+} during periods of flooding, leading to replacement of exchangeable cations

643   in the interlayers of clay minerals, and H^+ can be produced by re-oxidation of Fe^{2+},

644   involved in the formation of HIMs (Brinkman 1970). Another similarity is that paddy

645   soils also possess an A horizon like the HH in the QRS profiles. Compared to

646   underlying horizons, the A horizon is more sensitive to variations in local hydrology,

647   responding to seasonal wet-dry cycles that promote development of

648   hydroxy-intercalated interlayers (Rich 1968). In contrast, the HH in the QRS profiles

649   may have formed in a more oxic environment than the A horizon of paddy soils due to

650   better-drained soil conditions with a greater abundance of acidic cations to maintain

651   acidic weathering, favoring formation of HIMs (Rich 1968; Georgiadis et al. 2020). As

652   discussed above, the RH also formed in a seasonal wet-dry environment, yet HIMs

653   have not been found in the RH due to insufficient acidic cations as well as more

654   frequent redox oscillations of iron (i.e., strong ferrolysis) in macrosites (Fig. 2b).

655

656   **Redox and weathering intensity through the Songzi soil profile**

657   The HH, RH, and BL at Songzi are characterized by different weathering degrees,

658   redox conditions, soil acidities, and CECs, reflecting variation in the hydrologic

659   conditions in which mineral dissolution, transformation, and neogenesis took place.

660   The availability of chemical agents (i.e., oxygen, cations, and biota) and the pH and

661   redox potential of the aqueous solution are generally key factors influencing the soil

662   hydrologic regime (Kump et al. 2000; Chadwick and Chorover 2001).

663   Variations in the Ce anomaly can track soil-redox status (Laveuf and Cornu 2009;

664   Vázquez-Ortega et al. 2016; Chen et al. 2019). In the HH, consistently positive Ce

665   anomalies point to generally oxic conditions, whereas the BL exhibits slightly

666   negative Ce anomalies, denoting more anoxic conditions (Fig. 8i). The inferred

667   soil-redox conditions are consistent with the measured soil-redox potentials (Fig. 8d).

668   The RH is a highly redox-dynamic horizon with diagnostic redoximorphic features

669   (Fig. 2b). Fluctuating redox conditions can be achieved through hydrological

670   perturbations in aquatic environments (Peiffer et al. 2021). Plinthites and white veins

671   are regarded as Fe-enriched and Fe-depleted microsites produced through local redox

672   cycling (Coward et al. 2018; Chen et al. 2019). The occurrence of widespread

673   Fe-depleted veins in the RH suggests a more waterlogged condition than in the HH,

674   an inference supported by the minor negative Ce anomalies within this horizon (Fig.

675   8i).

676   Despite a certain degree of dynamic hydrologic evolution, the whole Songzi

677   profile experienced a continuous history of deposition and pedogenesis under

678   relatively uniform environmental conditions (Fig. S5), which is typical of QRS

679   profiles. These conditions included generally intense chemical weathering (CIA >

680   80 %), low organic accumulation (TOC < 2.5 g kg^{-1}), and a monsoonal climate

681   dominated by the East Asian monsoon system (Tables 2 and 4). The soil samples from

682   the Songzi and Xuancheng (XC) profiles exhibit similar compositions in a M^+-4Si-R^{2+}

683   ternary diagram, indicating similar weathering conditions (Fig. 7). Kaolinite and

684   Fe/Al-(hydr)oxides are found throughout the Songzi section, corresponding to

685   sustained, high-intensity post-depositional pedogenic processes. Compared with the

686   HH, the deeper RH-BL layers experienced more intense weathering, as denoted by

687   generally higher Δ4Si and CIA values (Fig. 8; Table 4).

688

689   **Secondary clay-mineral evolution coupled with soil hydrologic variation**

690   The composition of the clay-mineral assemblage at Songzi shows notable

691   variation along a depth profile (Fig. 8). Apart from clay-sized illite that can be

692   considered a detrital mineral of eolian origin (cf. Churchman and Lowe 2012),

693   multiple secondary clay minerals are present, including HIV, I-S, K-S, smectite, and

694 kaolinite (Figs. 3 and 8). In Figure 8a, we illustrate possible transformation pathways

695 of clay minerals in horizons characterized by a range of hydroclimatic conditions. The

696 presence of interstratified clays indicates the progressive transformation from one

697 compositional endmember to the other. For example, the presence of I-S (or I-V) in

698 the Songzi samples is indicative of transformation of illite to smectite (or vermiculite),

699 as commonly reported in soil environments (Hong et al. 2014; Andrade et al. 2019).

700 These interstratified clay minerals can be further transformed to pure smectite or

701 vermiculite through continued weathering. Andrade et al. (2019) suggested that the

702 transformation to smectite or vermiculite are dependent on the relative contents of Mg

703 and Al in the parent rocks.

704 In the HH, primary minerals were transformed to kaolinite with vermiculite

705 group minerals (i.e., HIV) as intermediate products, whereas in the RH-BL, primary

706 minerals tended to be transformed into smectite group minerals. The XRD spectra of

707 the RH samples show no peaks at ~14 Å, indicating an absence of discrete expandable

708 2:1 clay minerals (i.e., smectite or vermiculite), although a certain amount of K-S is

709 present (Figs. 3 and S1). K-S is commonly viewed as an intermediate product of

710 progressive kaolinization of smectite, and the transformation of smectite to kaolinite

711 is indicative of increasing soil maturity (Churchman et al. 1994; Vingiani et al. 2004;

712 Fang et al. 2019). Discrete smectite minerals were detected only in the BL, i.e., the

713 most intensely weathered part of the Songzi profile (Figs. 3 and 8).

714 All Songzi soil samples exhibit similar REE distributions and nearly constant

715   La-Th concentrations (La/Th ranges from 2.10 to 2.53), suggesting a relatively

716   uniform primary composition for the entire section (Figs. S3 and S5). Thus, the

717   diversity of clay types present in this soil profile can be ascribed to the dynamic

718   nature of the local hydroclimate. The HH is characterized by oxic conditions and

719   abundant active acid cations, favoring formation of vermiculite group minerals,

720   especially HIV (see preceding section for details). K-S preferentially occurs in

721   horizons that are slightly anoxic and poorly drained. In well-drained soils subject to

722   intense chemical weathering, smectite is completely transformed to kaolinite, so the

723   former mineral is rarely found in moist tropical soils except for those subject to

724   seasonal wet-dry climate cycles (Fisher and Ryan 2006; Ryan and Huertas 2009;

725   Hong et al. 2012; Fang et al. 2019). The RH experienced annual redox oscillations

726   linked to wet-dry cycles, i.e., conditions that were favorable for K-S preservation. The

727   BL contains a higher proportion of SiO_2 and lower proportions of alkali and

728   alkaline-earth metals compared to the HH and RH, reflecting intense hydrolysis. In

729   extreme weathering environments, kaolinite and K-S are the most stable phyllosilicate

730   species, and they are the dominant secondary clay phases in the BL (kaolinite + K-S ≥

731   62 %; Table S3). The BL has relatively high pH (≥ 6.3) and an effective CEC of 100 %

732   saturation with base cations, favoring the formation of smectite group minerals (Fig.

733   9c; Table 2). We infer that an aquic moisture regime and near-neutral soil pH played

734   key roles in smectite formation in the study section.

735

IMPLICATIONS

736

737   A red soil profile with evident redoximorphic features was investigated with a

738   focus on clay-mineral transformations using integrated physico-chemical,

739   mineralogical, geochemical, and spectral analyses. Our investigation shows a

740   coupling between clay-mineral evolution and soil redoximorphic changes within a red

741   soil section. Our investigation also shows that, from the primary minerals to the final

742   weathering products, the transformation pathway is mainly mediated by key hydrologic

743   factors such as the acidic cation concentration in soil solutions, waterlogging, and

744   redox oscillations. We suggest that soil hydrologic conditions are tightly coupled with

745   the decomposition and recombination of secondary minerals, especially HIV, smectite

746   and interstratified smectitic clay minerals. HIV is favored in oxic, well-drained soil

747   systems, in which the aqueous solution has adequate acidic cations to promote chemical

748   weathering. When soils are more waterlogged and the aqueous solution is dominated by

749   base cations, detrital minerals tend to transform to smectite group minerals. Particular

750   emphasis is given to the important role of the soil acidic pool (including both H^+ ions

751   and other acidic cations) in inducing transformations to hydroxy-interlayered clay

752   minerals. This study advances our understanding on the transformation processes

753   between different clay minerals and their environmental controls in natural soil

754   systems. The close relationship between hydrologic conditions and secondary clay

755   alteration confirmed in this study provides new insights into the kinetics of

756   water-mineral interactions that are central to all geological processes.

772

REFERENCES CITED

774   Aguiar, N. O., Novotny, E. H., Oliveira, A. L., Rumjanek, V. M., Olivares, F. L., and

775   Canellas, L. P. (2013) Prediction of humic acids bioactivity using spectroscopy

776   and multivariate analysis. Journal of Geochemical Exploration, 129, 95-102.

777   Andrade, G.R.P., Cuadros, J., Partiti, C.S.M., Cohen, R., and Vidal-Torrado, P. (2018)

778   Sequential mineral transformation from kaolinite to Fe-illite in two Brazilian

779   mangrove soils. Geoderma, 309, 84-99.

780   Andrade, G.R.P., Azevedo, A.C.D., Lepchak, J.K., and Assis, T.C. (2019) Weathering

781   of Permian sedimentary rocks and soil clay minerals transformations under

782   subtropical climate, southern Brazil (Paraná State). Geoderma, 336, 31-48.

783   Araki, S., and Kyuma, K. (1986) Chemical and clay mineralogical characteristics of red

784   and/or yellow colored soil materials in relation to lithology and weathering indices.

785   Soil Science and Plant Nutrition, 32, 265-271.

786   Baes, A.U., and Bloom, P.R. (1989) Diffuse reflectance and transmission Fourier

787   transform infrared (DRIFT) spectroscopy of humic and fulvic acids. Soil Science

788   Society of America Journal, 53, 695-700.

789   Barnhisel, R.I., and Bertsch, P.M. (1989) Chlorites and Hydroxy-Inter layered

790   vermiculite and smectite. In Dixon, J. B., Weed, S. B. (eds.): Minerals in Soil

791   Environments. SSSA, Madison, WI, USA, pp. 729–788.

792   Barnhisel, R.I., and Rich, C.I. (1963) Gibbsite formation from aluminum-interlayers in

793   montmorillonite. Soil Science Society of America Proceedings, 27, 632-635.

794   Blume, H. P., and Schwertmann, U. (1969) Genetic evaluation of profile distribution of

795   aluminum, iron, and manganese oxides. Soil Science Society of America Journal,

796   33, 438-444.

797   Bockheim, J.G. (2014) Soil Geography of the USA: A Diagnostic-Horizon Approach.

798   Springer International Publishing, Switzerland.

799   Brinkman, R., 1970. Ferrolysis, a hydromorphic soil forming process. Geoderma, 3,

800   199-206.

801   Calderón, F., Haddix, M., Conant, R., Magrini-Bair, K., and Paul, E. (2013) Diffuse

802   reflectance Fourier Transform mid-infrared spectroscopy as a method of

803   characterizing changes in soil organic matter. Soil Science Society of America

804   Journal, 77, 1591-1600.

805   Carstea, D.D., Harward, M.E., and Knox, E.G. (1970) Comparison of iron and

806   aluminum hydroxy interlayers in montmorillonite and vermiculite: I. Formation.

807   Soil Science Society of America Journal, 34, 517-521.

808   Chadwick, O.A., and Chorover, J. (2001) The chemistry of pedogenic thresholds.

809   Geoderma, 100, 321-353.

810   Chen, C., Barcellos, D., Richter, D.D., Schroeder, P.A., and Thompson, A. (2019)

811   Redoximorphic Bt horizons of the Calhoun CZO soils exhibit depth-dependent

812   iron-oxide crystallinity. Journal of Soils and Sediments, 19, 785-797.

813   Chen, J., An, Z.S., Liu, L.W., Ji, J.F., Yang, J.D., and Chen, Y. (2001) Variations in

814   chemical compositions of the eolian dust in Chinese Loess Plateau over the past

815   2.5 Ma and chemical weathering in the Asian inland. Science in China D—Earth

816   Sciences, 44, 403-413.

817   Chorover, J., Amistadi, M.K., and Chadwick, O.A. (2004) Surface charge evolution of

818   mineral-organic complexes during pedogenesis in Hawaiian basalt. Geochimica et

819   Cosmochimica Acta, 68, 4859-4876.

820   Chorover, J., Kretzschmar, R., Garcia-Pichel, F., and Sparks, D.L. (2007) Soil

821   biogeochemical processes within the Critical Zone. Elements, 3, 321-326.

822   Churchman, G.J. (2018) Game Changer in Soil Science. Functional role of clay

823   minerals in soil. Journal of Plant Nutrition and Soil Science, 181, 99-103.

824   Churchman, G.J., and Lowe, D.J. (2012) Alteration, formation, and occurrence of

825   minerals in soils. In: Huang, P.M., Li, Y., and Summer, M.E. (eds.) Handbook of

826   Soil Sciences, 2nd ed., Vol. 1: Properties and Processes. CRC Press, Boca Raton,

827   Florida, pp. 20.1-20.72.

828   Churchman, G.J., Slade, P.G., Self, P.G., and Janik, L.J. (1994) Nature of interstratified

829   kaolin-smectites in some Australian soils. Australian Journal of Soil Research, 32,

830   805-822.

831   Compton, J.S., White, R.A., and Smith, M. (2003) Rare earth element behavior in soils

832   and salt pan sediments of a semi-arid granitic terrain in the Western Cape, South

833   Africa. Chemical Geology, 201, 239-255.

834   Coward, E.K., Thompson, A.T., and Plante, A.F. (2017) Iron-mediated mineralogical

835   control of organic matter accumulation in tropical soils. Geoderma, 306, 206-216.

836   Coward, E.K., Thompson, A., and Plante, A.F. (2018) Contrasting Fe speciation in two

837   humid forest soils: Insight into organomineral associations in redox-active

838   environments. Geochimica et Cosmochimica Acta, 238, 68-84.

839   Cuadros, J. and Altaner, S.P. (1998) Characterization of mixed-layer illite-smectite

840   from bentonites using microscopic, chemical, and X-ray methods; constraints on

841   the smectite-to-illite transformation mechanism. The American mineralogist, 83,

842   762-774.

843   Cuadros, J. and Dudek, T. (2006) FTIR investigation of the evolution of the octahedral

844   sheet of kaolinite-smectite with progressive kaolinization. Clays and clay minerals,

845   54, 1-11.

846   Cuadros, J., Cesarano, M., Dubbin, W., Smith, S.W., Davey, A., Spiro, B., Burton,

847   R.G.O., and Jungblut, A.D. (2018) Slow weathering of a sandstone-derived

848   Podzol (Falkland Islands) resulting in high content of a non-crystalline silicate.

849   American Mineralogist, 103, 109-124.

850   Deng, Y., Li, H., Wang, Y., Duan, Y., and Gan, Y. (2014) Temporal variability of

851   groundwater chemistry and relationship with water-table fluctuation in the

852   Jianghan Plain, central China. Procedia Earth and Planetary Science, 10, 100-103.

853   Dietel, J., Gröger-Trampe, J., Bertmer, M., Kaufhold, S., Ufer, K., and Dohrmann, R.

854   (2019a) Crystal structure model development for soil clay minerals-I.

855   Hydroxy-interlayered smectite (HIS) synthesized from bentonite. A

856   multi-analytical study. Geoderma, 347, 135-149.

857   Dietel, J., Ufer, K., Kaufhold, S., and Dohrmann, R. (2019b) Crystal structure model

858   development for soil clay minerals-II. Quantification and characterization of

859   hydroxy-interlayered smectite (HIS) using the Rietveld refinement technique.

860   Geoderma, 347, 1-12.

861   Ding, Y.H., and Chan, J. (2005) The East Asian summer monsoon: an overview.

862   Meteorology and Atmospheric Physics, 89, 117-142.

863   Dong, H. (2012) Clay-microbe interactions and implications for environmental

864   mitigation. Elements, 8, 113-118.

865   Dudek, T., Cuadros, J., and Huertas, J. (2007) Structure of mixed-layer

866   kaolinite-smectite and smectite-to-kaolinite transformation mechanism from

867   synthesis experiments. American Mineralogist, 92, 179-192.

868   Ellerbrock, R.H., Höhn, A., and Gerke, H.H. (1999) Characterization of soil organic

869   matter from a sandy soil in relation to management practice using FT-IR

870   spectroscopy. Plant and Soil, 213, 55-61.

871   Essington, M.E. (2015) Soil and Water Chemistry: An Integrative Approach, 2nd ed.

872   CRC Press, Boca Raton, Florida, 539 pp.

873   Evangelou, V.P., and Phillips, R.E. (2005) Cation exchange in soils. In: M.A. Tabatabai,

874   and D.L. Sparks (eds.), Chemical Processes in Soils, 8, 343-410.

875   Fang, Q., Hong, H., Zhao, L., Furnes, H., Lu, H., Han, W., Liu, Y., Jia, Z., Wang, C.,

876   Yin, K., and Algeo, T.J. (2017) Tectonic uplift-influenced monsoonal changes

877   promoted hominin occupation of the Luonan Basin: Insights from a loess-paleosol

878   sequence, eastern Qinling Mountains, central China. Quaternary Science Reviews,

879   169, 312-329.

880   Fang, Q., Hong, H., Algeo, T.J., Huang, X., Sun, A., Churchman, G.J., Chorover, J.,

881   Chen, S., and Liu, Y. (2019) Microtopography-mediated hydrologic environment

882   controls elemental migration and mineral weathering in subalpine surface soils of

883   subtropical monsoonal China. Geoderma, 344, 82-98.

884   Fisher, G.B., and Ryan, P.C. (2006) The smectite to disordered kaolinite transition in a

885   tropical soil chronosequence, Pacific Coast, Costa Rica. Clays and Clay Minerals,

886   54, 571-586.

887   Gallet, S., Jahn, B., and Torii, M. (1996) Geochemical characterization of the Luochuan

888   loess-paleosol sequence, China, and paleoclimatic implications. Chemical

889   Geology, 133, 67-88.

890   Gan, Y., Wang, Y., Duan, Y., Deng, Y., Guo, X., and Ding, X. (2014)

891   Hydrogeochemistry and arsenic contamination of groundwater in the Jianghan

892   Plain, central China. Journal of Geochemical Exploration, 138, 81-93.

893   Georgiadis, A., Dietel, J., Dohrmann, R., and Rennert, T. (2020) What are the nature

894   and formation conditions of hydroxy-interlayered minerals (HIMs) in soil?

895   Journal of Plant Nutrition and Soil Science, 183, 12-26.

896   Goodfellow, B.W., Hilley, G.E., Webb, S.M., Sklar, L.S., Moon, S., and Olson, C.A.

897   (2016) The chemical, mechanical, and hydrological evolution of weathering

898   granitoid. Journal of Geophysical Research: Earth Surface, 121, 1410-1435.

899   Graham, R.C., Weed, S.B., Bowen, L.H., and Buol, S.W. (1989) Weathering of

900   iron-bearing minerals in soils and saprolite on the North Carolina Blue Ridge

901   Front: I. Sand-size primary minerals. Clays and clay minerals, 37, 19-28.Hall, S.J.,

902   Berhe, A.A., and Thompson, A. (2018) Order from disorder: do soil organic

903   matter composition and turnover co-vary with iron phase crystallinity?

904   Biogeochemistry, 140, 93-110.

905   Han, L., Hao, Q., Qiao, Y., Wang, L., Peng, S., Li, N., Gao, X., Fu, Y., Xu, B., and Gu, Z.

906   (2019) Geochemical evidence for provenance diversity of loess in southern China

907   and its implications for glacial aridification of the northern subtropical region.

908   Quaternary Science Reviews, 212, 149-163.

909   Harsh, J., Chorover, J., and Nizeyimana, E. (2002) Allophane and imogolite. J.B. Dixon,

910   and D.G. Schulze (eds.), Soil Mineralogy with Environmental Applications, 7, pp.

911   291-322.

912   He, H., Ji, S., Tao, Q., Zhu, J., Chen, T., Liang, X., Li, Z., and Dong, H. (2017)

913   Transformation of halloysite and kaolinite into beidellite under hydrothermal

914   condition. American Mineralogist, 102, 997-1005.

915   He, X., Xie, W., Deng, S., and Lu, S. (1983) The problems and achievements about

916   improving use red-yellow soil in China. Journal of Soil Science, 2, 1-4 (Chinese

917   context with English abstract).

918   Hersbach, H., Bell, B., Berrisford, P., Biavati, G., Horányi, A., Muñoz Sabater, J.,

919   Nicolas, J., Peubey, C., Radu, R., Rozum, I., Schepers, D., Simmons, A., Soci, C.,

920   Dee, D., and Thépaut, J-N. (2019) ERA5 monthly averaged data on single levels

921   from 1979 to present. Copernicus Climate Change Service (C3S) Climate Data

922   Store (CDS), DOI: 10.24381/cds.f17050d7.

923   Hong, H., Churchman, G.J., Gu, Y., Yin, K., and Wang, C. (2012) Kaolinite-smectite

924   mixed-layer clays in the Jiujiang red soils and their climate significance.

925   Geoderma, 173, 75-83.

926   Hong, H., Churchman, G.J., Yin, K., Li, R., and Li, Z. (2014) Randomly interstratified

927   illite-vermiculite from weathering of illite in red earth sediments in Xuancheng,

928   southeastern China. Geoderma, 214-215, 42-49.

929   Hong, H., Cheng, F., Yin, K., Churchman, G.J., and Wang, C. (2015) Three-component

930   mixed-layer illite/smectite/kaolinite (I/S/K) minerals in hydromorphic soils, south

931   China. American Mineralogist, 100, 1883-1891.

932   Hong, H., Fang, Q., Cheng, L., Wang, C., and Churchman, G.J. (2016)

933   Microorganism-induced weathering of clay minerals in a hydromorphic soil.

934   Geochimica et Cosmochimica Acta, 184, 272-288.

935   Hsu, P.H. (1989) Aluminum hydroxides and oxyhydroxides. In: J.B. Dixon, and S.B.

936   Weed (eds.), Minerals in Soil Environments, vol. 1, 2nd ed., pp. 331-378.

937   Hu, X., Wei, J., Du, Y., Xu, L., Wang, H., Zhang, G., Ye, W., and Zhu, L. (2010)

938   Regional distribution of the Quaternary Red Clay with aeolian dust characteristics

939   in subtropical China and its paleoclimatic implications. Geoderma, 159, 317-334.

940   Hu, X., Du, Y., Liu, X., Zhang, G., Jiang, Y., and Xue, Y. (2015) Polypedogenic case of

941   loess overlying red clay as a response to the Last Glacial–Interglacial cycle in

942   mid-subtropical Southeast China. Aeolian Research, 16, 125-142.

943   Huang, C., Wang, M., Tan, W., Wang, M., and Koopal, L.K. (2018)

944   Hydroxy-interlayered minerals in the Holocene paleosol on the southernmost

945   Loess Plateau, China. Applied Clay Science, 153, 70-77.

946   Jin, L., Ravella, R., Ketchum, B., Bierman, P.R., Heaney, P., White, T., and Brantley,

947   S.L. (2010) Mineral weathering and elemental transport during hillslope evolution

948   at the Susquehanna/Shale Hills Critical Zone Observatory. Geochimica et

949   Cosmochimica Acta, 74, 3669-3691.

950   Jin, L., Andrews, D.M., Holmes, G.H., Lin, H., and Brantley, S.L. (2011) Opening the

951   "black box": water chemistry reveals hydrological controls on weathering in the

952   Susquehanna Shale Hills Critical Zone Observatory. Vadose Zone Journal, 10,

953   928-942.

954   Konert, M., and Vandenberghe, J. (1997) Comparison of laser grain size analysis with

955   pipette and sieve analysis: a solution for the underestimation of the clay fraction.

956   Sedimentology, 44, 523-535.

957   Korchagin, J., Bortoluzzi, E.C., Moterle, D.F., Petry, C., and Caner, L. (2019)

958   Evidences of soil geochemistry and mineralogy changes caused by eucalyptus

959   rhizosphere. Catena, 175, 132-143.

960   Kottek, M., Grieser, J., Beck, C., Rudolf, B., and Rubel, F. (2006) World Map of the

961   Köppen-Geiger climate classification updated. Meteorol. Z., 15, 259-263.

962   Kump, L.R., Brantley, S.L., and Arthur, M.A. (2000) Chemical weathering,

963   atmospheric CO_2, and climate. Annual Review of Earth and Planetary Sciences,

964   28, 611-667.

965   Kundzewicz, Z.W., Huang, J., Pinskwar, I., Su, B., Szwed, M., and Jiang, T. (2020)

966   Climate variability and floods in China—A review. Earth-Science Reviews, 211,

967   103434.

968   Kyuma, K. (1978) Mineral Composition of Rice Soils, in IRRI (ed.): Soil and Rice.

969   International Rice Research Institute, Los Banos, Philippines, pp. 219–235.

970   Laveuf, C., and Cornu, S. (2009) A review on the potentiality of Rare Earth Elements to

971   trace pedogenetic processes. Geoderma, 154, 1-12.

972   Li, S., He, H., Tao, Q., Zhu, J., Tan, W., Ji, S., Yang, Y. and Zhang, C. (2020)

973   Kaolinization of 2:1 type clay minerals with different swelling properties.

974   American Mineralogist, 105, 687-696.

975   Ma, L., Zhu, J., He, H., Xi, Y., Zhu, R., Tao, Q., and Liu, D. (2015) Thermal analysis

976   evidence for the location of zwitterionic surfactant on clay minerals. Applied Clay

977   Science, 112-113, 62-67.

978   Madeira, M., Auxtero, E., and Sousa, E. (2003) Volcanic soils: properties and processes

979   as a function of soil genesis and land use. Cation and anion exchange properties of

980   Andisols from the Azores, Portugal, as determined by the compulsive exchange

981   and the ammonium acetate methods. Geoderma, 117, 225-241.

982   Madejová, J. (2003) FTIR techniques in clay mineral studies. Vibrational Spectroscopy,

983   31, 1-10.

984   Mavris, C., Cuadros, J., Nieto, J.M., Bishop, J.L., and Michalski, J.R. (2018) Diverse

985   mineral assemblages of acidic alteration in the Rio Tinto area (southwest Spain):

986   Implications for Mars. American Mineralogist, 103, 1877-1890.

987   McLennan, S.M. (2001) Relationships between the trace element composition of

988   sedimentary rocks and upper continental crust. Geochemistry, Geophysics,

989   Geosystems, 2, 2000GC000109.

990   Meunier, A. (2007) Soil hydroxy-interlayered minerals: a re-interpretation of their

991   crystallochemical properties. Clays and Clay Minerals, 55, 380-388.

992   Meunier, A., Caner, L., Hubert, F., El Albani, A., and Pret, D. (2013) The weathering

993   intensity scale (WIS): An alternative approach of the Chemical Index of Alteration

994   (CIA). American Journal of Science, 313, 113-143.

995   Mitsuchi, M., 1974. Chloritization in lowland paddy soils. Soil science and plant

996   nutrition (Tokyo), 20, 107-116.

997   Moore, D.M., and Reynolds, R.C. (1997) X-ray Diffraction and the Identification and

998   Analysis of Clay Minerals. Oxford University Press Inc., USA, pp. 100-200.

999   Ndzana, G.M., Huang, L., Wang, J.B., and Zhang, Z.Y. (2018) Characteristics of clay

1000   minerals in soil particles from an argillic horizon of Alfisol in central China.

1001   Applied Clay Science, 151, 148-156.

1002   Nesbitt, H.W., and Young, G.M. (1982) Early Proterozoic climates and plate motions

1003   inferred from major element chemistry of lutites. Nature, 299, 715-717.

1004   Nguyen, T.T., Janik, L.J., and Raupach, M. (1991) Diffuse reflectance infrared Fourier

1005   transform (DRIFT) spectroscopy in soil studies. Soil Research, 29, 49-67.

1006   Nuzzo, A., Buurman, P., Cozzolino, V., Spaccini, R., and Piccolo, A. (2020) Infrared

1007   spectra of soil organic matter under a primary vegetation sequence. Chemical and

1008   Biological Technologies in Agriculture, 7, 1-12.

1009   Parfitt, R.L., and Childs, C.W. (1988) Estimation of forms of Fe and Al: A review, and

1010   analysis of contrasting soils by dissolution and Mossbauer methods. Soil Research,

1011   26, 121-144.

1012   Peiffer, S., Kappler, A., Haderlein, S.B., Schmidt, C., Byrne, J.M., Kleindienst, S., Vogt,

1013   C., Richnow, H.H., Obst, M., Angenent, L.T., Bryce, C., McCammon, C., and

1014   Planer-Friedrich, B. (2021) A biogeochemical-hydrological framework for the

1015   role of redox-active compounds in aquatic systems. Nature Geoscience, 14,

1016   264-272.

1017   Pincus, L.N., Ryan, P.C., Huertas, F.J., and Alvarado, G.E. (2017) The influence of soil

1018   age and regional climate on clay mineralogy and cation exchange capacity of

1019   moist tropical soils: A case study from Late Quaternary chronosequences in Costa

1020   Rica. Geoderma, 308, 130-148.

1021   Rasmussen, C., Dahlgren, R.A., and Southard, R.J. (2010) Basalt weathering and

1022   pedogenesis across an environmental gradient in the southern Cascade Range,

1023   California, USA. Geoderma, 154, 473-485.

1024   Rennert, T. (2019) Wet-chemical extractions to characterise pedogenic Al and Fe

1025   species—A critical review. Soil Research, 57, 1-12.

1026   Rich, C.I. (1968) Hydroxy-interlayers in expansible layer silicates. Clays and Clay

1027   Minerals, 16, 15-30.

1028   Righi, D., Terribile, F., and Petit, S. (1999) Pedogenic formation of kaolinite-smectite

1029   mixed layers in a soil toposequence developed from basaltic parent material in

1030   Sardinia (Italy). Clays and clay minerals, 47, 505-514.

1031   Ryan, P.C., and Huertas, F.J. (2009) The temporal evolution of pedogenic Fe-smectite

1032   to Fe-kaolin via interstratified kaolin-smectite in a moist tropical soil

1033   chronosequence. Geoderma, 151, 1-15.

1034   Shang, C., and Zelazny, L.W. (2008) Selective dissolution techniques for mineral

1035   analysis of soil and sediments. In: Ulery, A.L. and Drees, L.R. (eds.) Methods of

1036   Soil Analysis, Part 5. Soil Science Society of America, Madison, Wisconsin, pp.

1037   33-80.

1038   Singer, A. (1980) The paleoclimatic interpretation of clay minerals in soils and

1039   weathering profiles. Earth-Science Reviews, 15, 303-326.

1040   Soil Survey Staff (2010) Keys to Soil Taxonomy, 11th Ed. USDA. National Resources

1041   Conservation Service, National Soil Survey Center, Lincoln, Nebraska, 338 pp.

1042   Sposito, G. (2008) The Chemistry of Soils, 2nd Ed. Oxford University Press,

1043   NewYork/UK, 329 pp.

1044   Szymański, W., Skiba, M., Nikorych, V.A., and Kuligiewicz, A. (2014) Nature and

1045   formation of interlayer fillings in clay minerals in Albeluvisols from the

1046   Carpathian Foothills, Poland. Geoderma, 235-236, 396-409.

1047   Thompson, A., Chadwick, O.A., Rancourt, D.G., and Chorover, J. (2006) Iron-oxide

1048   crystallinity increases during soil redox oscillations. Geochimica et

1049   Cosmochimica Acta, 70, 1710-1727.

1050   Vázquez-Ortega, A., Huckle, D., Perdrial, J., Amistadi, M.K., Durcik, M., Rasmussen,

1051   C., McIntosh, J., and Chorover, J. (2016) Solid-phase redistribution of rare earth

1052   elements in hillslope pedons subjected to different hydrologic fluxes. Chemical

1053   Geology, 426, 1-18.

1054   Vingiani, S., Righi, D., Petit, S., and Terribile, F. (2004) Mixed-layer kaolinite-smectite

1055   minerals in a red-black soil sequence from basalt in Sardinia, (Italy). Clays and

1056   Clay Minerals, 52, 473-483.

1057   Wakatsuki, T., Ishikawa, I., Araki, S., Kyuma, K. (1984) Changes in clay mineralogy in

1058   a chronosequence of polder paddy soils from Kojima Basin, Japan. Soil science

1059   and plant nutrition, 30, 25-38.

1060   Weil, R.R., and Brady, N.C. (2017) The Nature and Properties of Soils, 15th Ed.,

1061   Prentice-Hall Press, New York.

1062   Wilson, M.J., He, Z.L., and Yang, X.O. (2004) The Red Soils of China: Their nature,

1063   management and utilization. Springer Science Business Media, New York.

1064   Wu, L.M., Tong, D.S., Zhao, L.Z., Yu, W.H., Zhou, C.H., and Wang, H. (2014) Fourier

1065   transform infrared spectroscopy analysis for hydrothermal transformation of

1066   microcrystalline cellulose on montmorillonite. Applied Clay Science, 95, 74-82.

1067   Ying, H., Feng, X., Zhu, M., Lanson, B., Liu, F., and Wang, X. (2020) Formation and

1068   transformation of schwertmannite through direct Fe^{3+} hydrolysis under various

1069   geochemical conditions. Environmental Science: Nano, 7, 2385-2398.

1070   Yuan, P., Wu, D. Q., He, H. P., and Lin, Z.Y. (2004) The hydroxyl species and acid sites

1071   on diatomite surface: a combined IR and Raman study. Applied Surface Science,

1072   227(1-4), 30-39.

1073   Zhang, Z.Y., Huang, L., Liu, F., Wang, M.K., Fu, Q.L., and Zhu, J. (2016)

1074   Characteristics of clay minerals in soil particles of two Alfisols in China. Applied

1075   Clay Science, 120, 51-60.

1076   Zhao, L., Hong, H., Fang, Q., Yin, K., Wang, C., Li, Z., Torrent, J., Cheng, F., and

1077   Algeo, T.J. (2017) Monsoonal climate evolution in southern China since 1.2 Ma:

1078   New constraints from Fe-oxide records in red earth sediments from the Shengli

1079   section, Chengdu Basin. Palaeogeography, Palaeoclimatology, Palaeoecology,

1080   473, 1-15.

1081   Zhou, Y., Wang, Y., Li, Y., Zwahlen, F., and Boillat, J. (2013) Hydrogeochemical

1082   characteristics of central Jianghan plain, China. Environmental Earth Sciences, 68,

1083   765-778.

1084

Table 1. Morphological description of the Songzi profile

Depth (m)	Horizon	Munsell color	Structure	Texture
0-0.3	Ap (HH)	Dark brown (7.5YR 3/4)	Fine granular	Silty loam
0.3-0.7	Bw (HH)	Dark yellowish brown (10YR 2/4)	Granular	Silty loam
0.7-1.0			Granular	Silty loam
1.0-1.2	Bt1 (HH)	Yellowish brown (10YR 5/6)	Very fine Blocky	Silty clay loam
1.3-1.5			Very fine Blocky	Silty clay loam
1.6-1.8			Fine Blocky	Silty clay loam
1.9-2.1			Fine Blocky	Silty clay loam
2.2-2.4	Bt2 (RH)	Yellowish yellow (5YR 8/6) matrix accompanied with black (7.5YR 2/0) linings, red (2.5YR 4/8) plinthites, and white (2.5Y 8/2) veins.	Blocky	Silty clay
2.6-2.8			Blocky	Silty clay
2.9-3.1			Blocky	Silty clay
3.2-3.4			Blocky	Silty clay
3.5-3.7			Blocky	Silty clay
3.8-4.0			Blocky	Silty clay
4.1-4.3			Blocky	Silty clay
4.4-4.6			Blocky	Silty clay
4.7-4.9			Blocky	Silty clay loam
5.0-5.2			Blocky	Silty clay loam
5.3-5.5			Blocky	Silty clay loam
5.6-5.8			Blocky	Silty clay loam
5.9-6.1	BC (BL)	Yellowish brown (10YR 5/6)	Blocky	Silty clay loam
6.2-6.4			Blocky	Silty clay loam
6.5-6.7			Blocky	Silty clay loam
6.8-7.2			Blocky	Silty loam

Table 2. Major physico-chemical attributes of the Songzi soils

Horizon	Depth	Soil fractions			TOC	TN	pH	Eh	Exchangeable cations					CEC	Al_{ex}/CEC
		Clay	Silt	Sand					Al	Ca	Na	Mg	K		
	m	volume %			g kg^{-1}			mV	mmol kg^{-1}						%
HH	0.30	24.5	72.6	2.9	2.1	0.7	4.8	403	1.95	8.73	2.07	9.97	2.87	25.60	7.63
	0.90	26.3	71.3	2.3	1.4	0.4	4.9	367	0.77	9.88	3.40	11.25	4.48	29.79	2.59
	1.20	35.5	61.3	3.1	1.2	0.5	5.3	347	0.40	11.53	2.84	11.93	3.90	30.61	1.32
	1.50	34.6	63.3	2.2	1.3	0.5	5.8	336	0.85	15.57	2.97	15.46	3.71	38.56	2.20
	1.80	28.0	68.3	3.3	1.3	0.5	5.3	309	0.20	14.78	2.58	14.64	3.74	35.93	0.56
RH	2.10	34.9	64.8	0.3	1.6	0.4	5.6	341	0.15	16.34	2.54	14.96	3.79	37.79	0.40
	2.40	38.6	58.4	2.3	1.0	0.4	5.7	322	0.15	17.35	2.40	14.26	4.45	38.61	0.38
	3.00	39.7	58.6	1.6	1.0	0.5	5.6	297	0.03	19.62	2.36	12.89	4.87	39.78	0.09
	3.30	41.2	56.9	1.9	1.1	0.5	6.4	319	0.31	18.88	2.70	11.24	4.86	37.99	0.81
	3.60	38.3	59.7	2.0	0.9	0.4	5.8	307	0.20	19.34	2.98	10.73	4.61	37.86	0.54
	3.90	38.8	59.5	1.7	1.3	0.5	6.0	295	0.12	12.78	3.42	9.48	6.47	32.28	0.38
	4.20	38.9	57.1	3.8	1.0	0.5	6.2	281	0.05	18.60	1.87	9.22	3.61	33.36	0.15
	4.50	36.9	56.5	5.2	1.1	0.5	6.1	294	0.04	18.37	2.08	8.72	3.97	33.18	0.13
	5.10	30.3	64.4	4.4	1.0	0.4	6.2	281	0.03	15.16	2.21	7.27	3.23	27.90	0.12
	5.40	35.1	61.0	3.6	1.1	0.3	6.1	307	0.01	19.42	3.71	8.08	8.23	39.45	0.03
BL	6.00	27.8	69.7	2.6	1.0	0.4	6.3	228	0.00	15.97	1.22	6.09	1.92	25.21	0.01
	6.90	23.5	72.9	2.9	0.7	0.3	6.5	274	0.03	15.30	1.06	5.36	2.68	24.44	0.14

Table 3. Major IR absorption bands and functional groups assignments for inorganic components

Band regions (cm^{-1})	Assignments	Reference
3699	OH stretching of phyllosilicates (i.e., Kaolinite)	
3650	OH stretching of phyllosilicates (i.e., Kaolinite)	Nguyen et al., 1991; Mavris et al., 2018
3625	OH stretching of phyllosilicates (i.e., Kaolinite and dioctahedral 2:1 minerals)	
Broad 3400	OH stretching of water molecules	Baes and Bloom, 1989; Chorover et al., 2004
Triplet in 2000-1700	Combination bands of quartz	Nguyen et al., 1991
1640	HOH deformation of adsorbed water	Calderón et al., 2013
Broad 1100-850	Si(Al)-O-Si(Al) stretching of phyllosilicates and hydrous oxides of Al and Fe	Harsh et al., 2002; Chorover et al., 2004
915	Al-O-H bending of phyllosilicates	
Doublet at 800 and 780	Si-O stretching of quartz	Madejová, 2003; Wu et al., 2014
754	Si-O perpendicular of phyllosilicates	
697	Si-O perpendicular of phyllosilicates and quartz	
540	Al-OH in the interlayer hydroxide sheet	Barnhisel and Bertsch, 1989

Table 4. Major elements, CIA, and calculation of the parameters in the WIS system

| Horizon	Depth	SiO_2	TiO_2	Al_2O_3	Fe_2O_3	MnO	MgO	CaO	Na_2O	K_2O	P_2O_5	LOI	CIA	4Si	M^+	R^{2+}	$\Delta 4Si$
	m						wt %									mmol	
HH	0.3	70.09	0.98	14.11	5.51	0.05	1.07	0.19	0.39	2.11	0.06	5.14	81.15	291.63	64.21	27.08	76.16
	0.9	70.46	1.03	14.24	5.67	0.11	0.93	0.16	0.32	2.21	0.06	4.81	81.65	293.20	62.66	24.45	77.09
	1.2	70.12	1.02	14.32	5.93	0.12	0.84	0.15	0.23	2.13	0.06	4.86	82.83	291.78	58.12	22.24	78.41
	1.5	67.10	0.99	15.96	6.68	0.12	0.98	0.18	0.22	2.44	0.07	5.36	82.67	279.21	65.53	25.66	75.38
	1.8	67.35	0.98	15.52	6.47	0.10	0.96	0.19	0.25	2.40	0.07	5.20	82.25	280.23	65.57	24.94	75.59
RH	2.1	67.48	1.01	15.80	6.51	0.11	1.00	0.21	0.20	2.41	0.08	5.42	82.57	280.78	65.30	26.07	75.45
	2.4	68.66	1.01	14.86	6.46	0.08	0.91	0.2	0.21	2.29	0.09	5.10	82.33	285.71	62.42	23.46	76.89
	3.0	68.83	1.02	15.10	6.47	0.08	0.80	0.22	0.14	2.11	0.09	5.13	83.80	286.39	57.14	20.75	78.62
	3.3	68.29	1.03	15.23	6.38	0.09	0.75	0.22	0.14	2.11	0.08	5.19	83.96	284.16	56.94	19.72	78.75
	3.6	69.36	1.03	14.60	6.07	0.11	0.74	0.22	0.13	2.06	0.08	4.93	83.73	288.60	55.52	19.58	79.35
	3.9	71.08	1.05	13.98	5.80	0.12	0.68	0.21	0.12	1.94	0.07	4.83	83.94	295.77	52.36	18.27	80.72
	4.2	69.83	1.05	14.66	5.98	0.07	0.67	0.22	0.10	1.93	0.07	5.05	84.64	290.56	52.09	17.50	80.68
	4.5	70.95	1.06	14.10	5.66	0.09	0.64	0.21	0.09	1.88	0.06	4.77	84.58	295.25	50.31	17.01	81.43
	5.1	72.17	1.04	13.40	5.58	0.09	0.63	0.22	0.10	1.85	0.06	4.53	83.96	300.30	50.10	16.74	81.79
	5.4	72.51	1.09	13.18	5.50	0.10	0.61	0.22	0.09	1.84	0.06	4.49	83.83	301.73	49.76	16.43	82.01
BL	6.0	74.22	1.08	12.46	5.13	0.06	0.55	0.21	0.09	1.67	0.05	4.32	84.30	308.83	45.44	14.33	83.79
	6.6	75.55	1.10	11.65	5.12	0.11	0.53	0.20	0.08	1.51	0.06	4.06	84.55	314.38	41.67	14.33	84.88
	6.9	75.03	1.09	11.80	5.45	0.05	0.52	0.21	0.08	1.49	0.06	4.19	84.79	312.21	41.45	13.67	85.00
	7.2	76.36	1.10	11.23	4.55	0.03	0.47	0.20	0.07	1.32	0.05	3.99	85.46	317.73	37.40	11.91	86.57
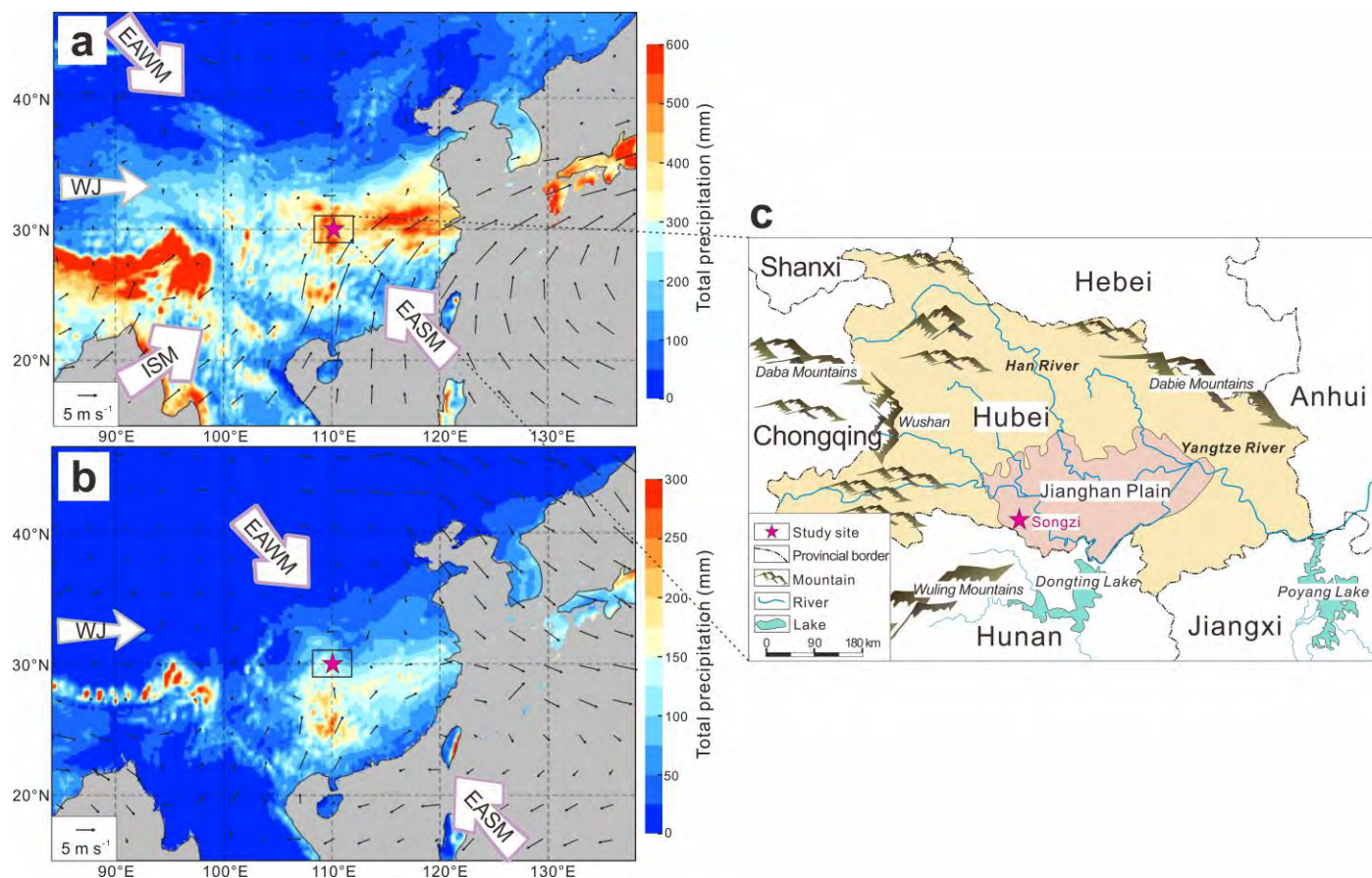
Figure 1. The major monsoon systems, precipitation (mm, shading) and 850-hPa winds (m s^{-1}, vectors) (data from European Center for Medium Weather Forecasting, the fifth generation ECMWF atmospheric reanalysis of the global climate; Hersbach et al., 2019) in the study area in a) June to July and b) January to February. c) Regional map showing the location and geologic setting of the Songzi section. ISM—Indian summer monsoon, EASM—East Asian summer monsoon, EAWM—East Asian winter monsoon, WJ—Westerly jet.
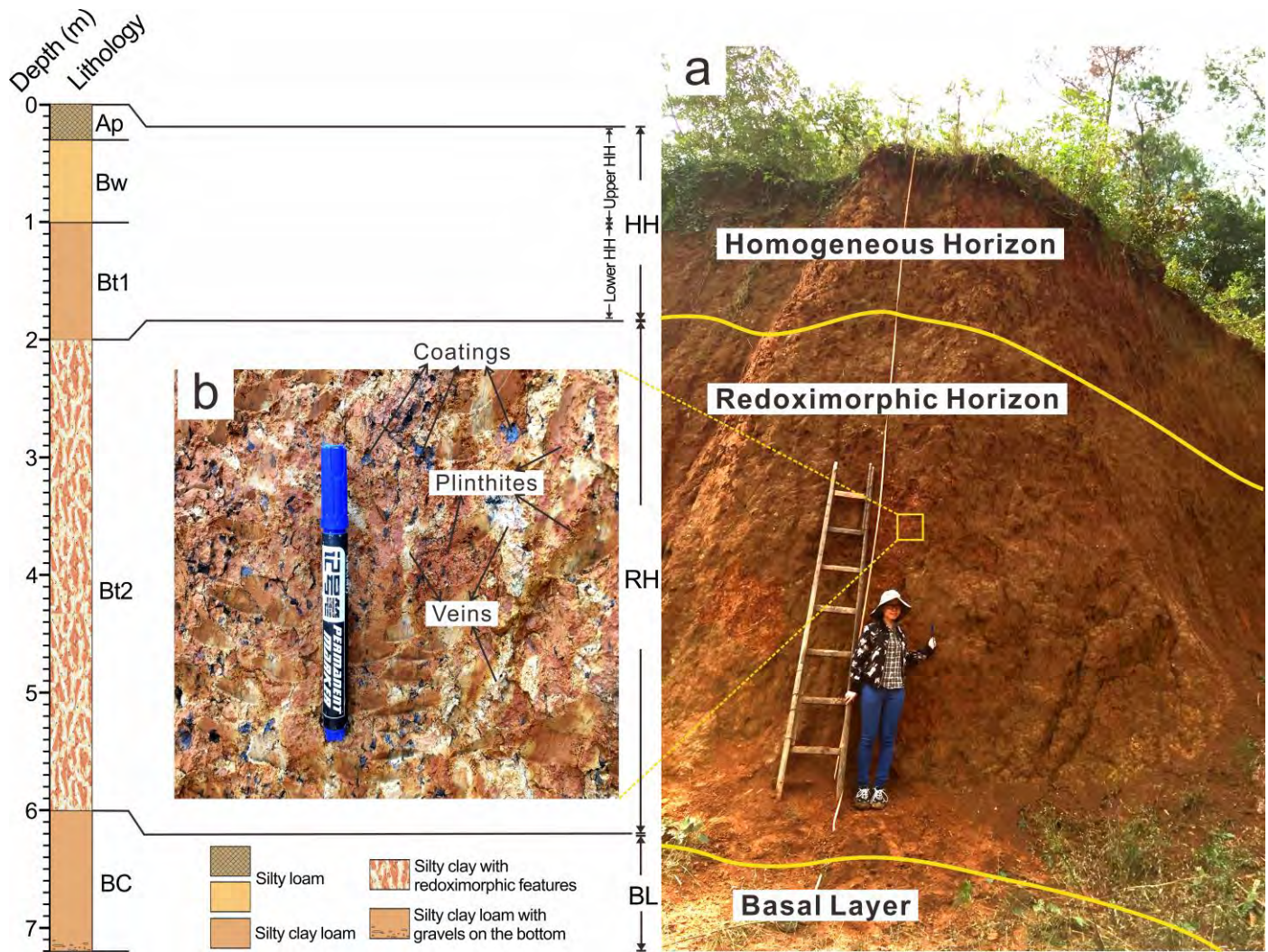
Figure 2. Field photos of the Songzi section. a) The Songzi section has depth-dependent horizons that contrast in texture, mineralogy, structure, and redoximorphic features. It can be divided into the upper homogeneous horizon (HH; 0-2 m), middle redoximorphic horizon (RH; 2.0-6.0 m), and the basal layer (BL; 6.0-7.2 m). b) Close-up of the redoximorphic features in the RH. The redoximorphic features include vivid red plinthite, white veins/mottles, and black coatings.
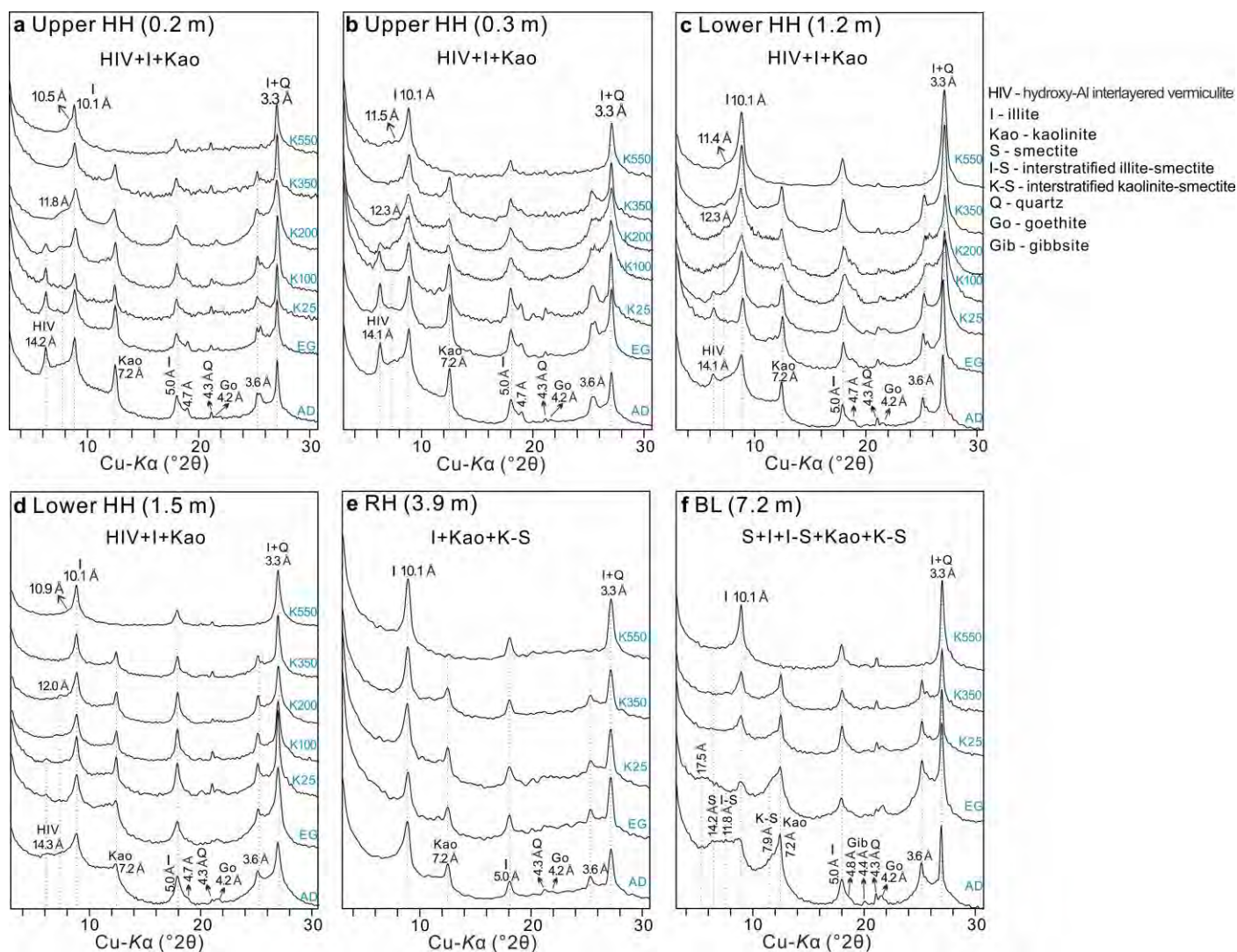
Figure 3. XRD patterns of representative soil samples from upper HH (a-b), lower HH (c-d), RH (e), and BL (f) of the Songzi section. AD = Air dried treatment; EG = ethylene glycol solvation; K25, K100, K200, K350, K550 = K-saturation at room temperature and heat treatment at 100, 200, 350, and 550 °C. Clay-mineral assemblages are shown above the XRD patterns, denoting the dominant clay minerals occurring in the corresponding soil horizon.
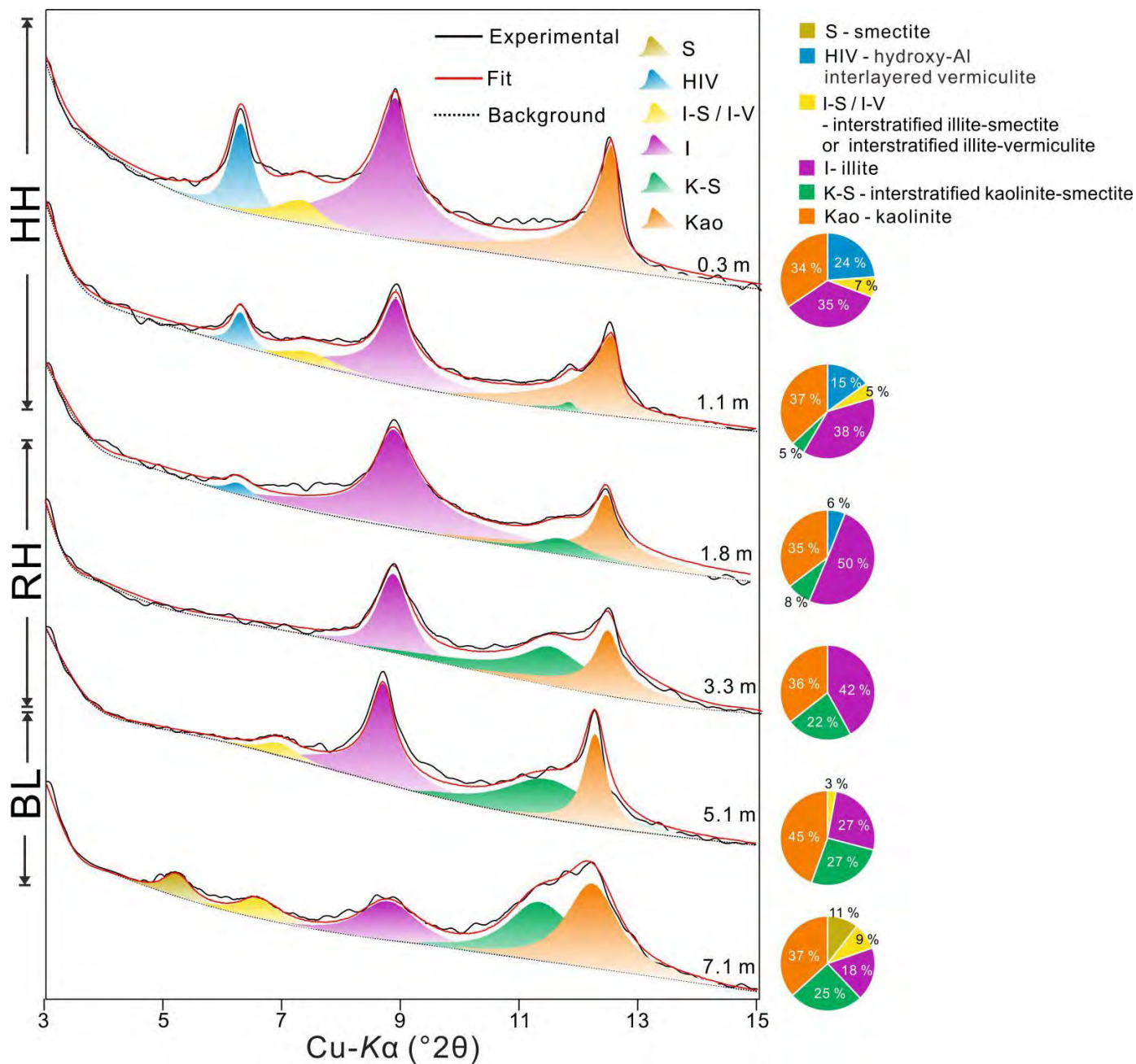
Figure 4. Results of XRD profile fitting for representative soil samples in HH, RH, and BL.
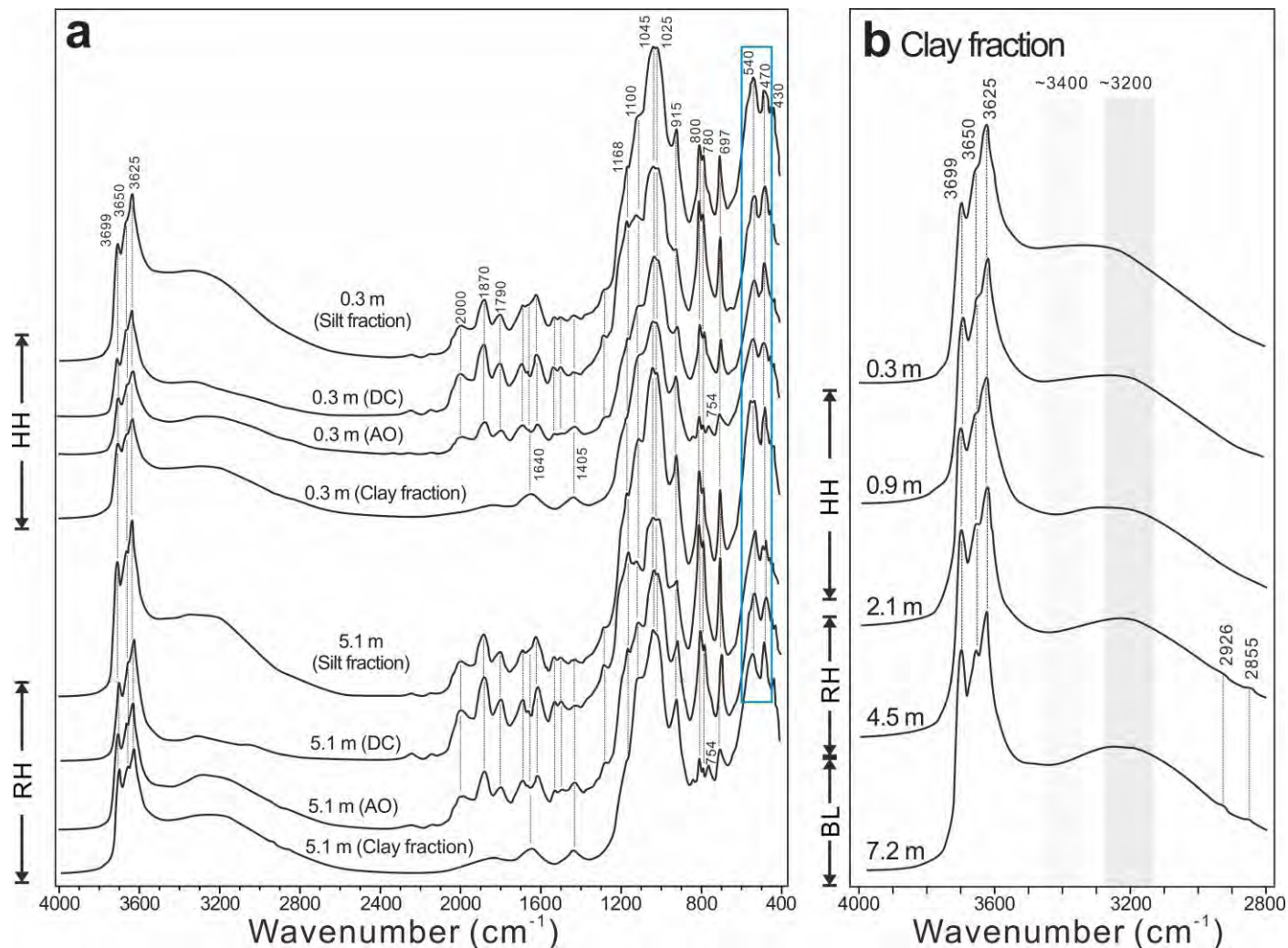
Figure 5. DRIFT spectra of representative samples in HH, RH, and BL. a) DRIFT spectra of HH soils and RH soils with various preparation techniques. DC: soil sample extracted in citrate-dithionite solution for 4 h; AO: soil sample extracted in acid ammonium oxalate solution for 4 h. b) DRIFT spectra of the clay fraction samples in the OH-stretching region. The most prominent features are those of kaolinite, 2:1 clay minerals, and quartz. For full assignment of the bands, see Table 3. Note that the bands may have been affected by some organic compounds.
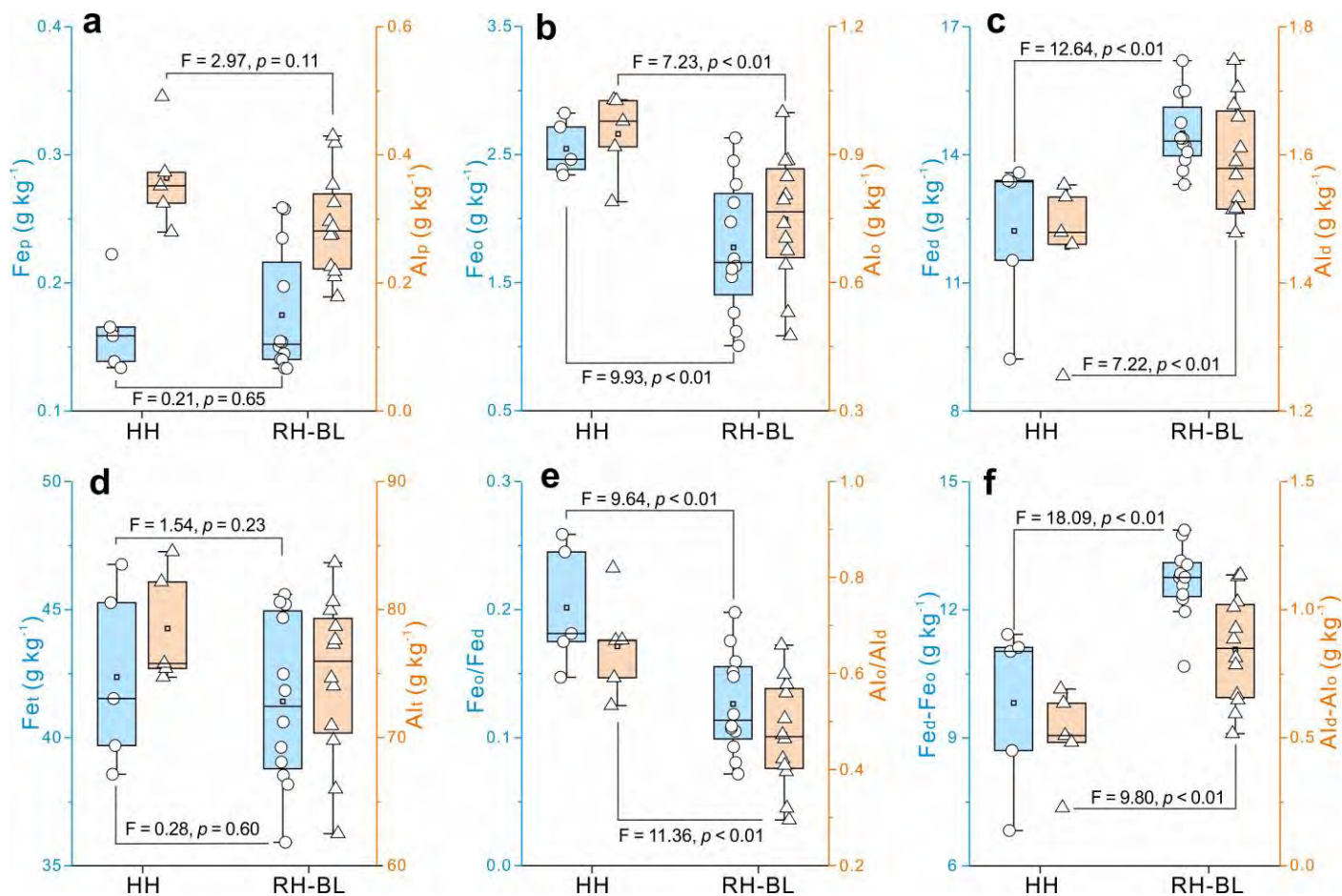
Figure 6. Extractable iron and aluminum in HH and RH-BL: a) Na-pyrophosphate extractable Fe (Fe_p) and Al (Al_p); b) ammonium-oxalate extractable Fe (Fe_o) and Al (Al_o); c) citrate-ascorbate extractable Fe (Fe_d) and Al (Al_d); d) total concentrations of Fe (Fe_t) and Al (Al_t); e) active ratio of Fe (Fe_o/Fe_d) and Al (Al_o/Al_d); and f) crystallinity of Fe (Fe_d-Fe_o) and Al (Al_d-Al_o).
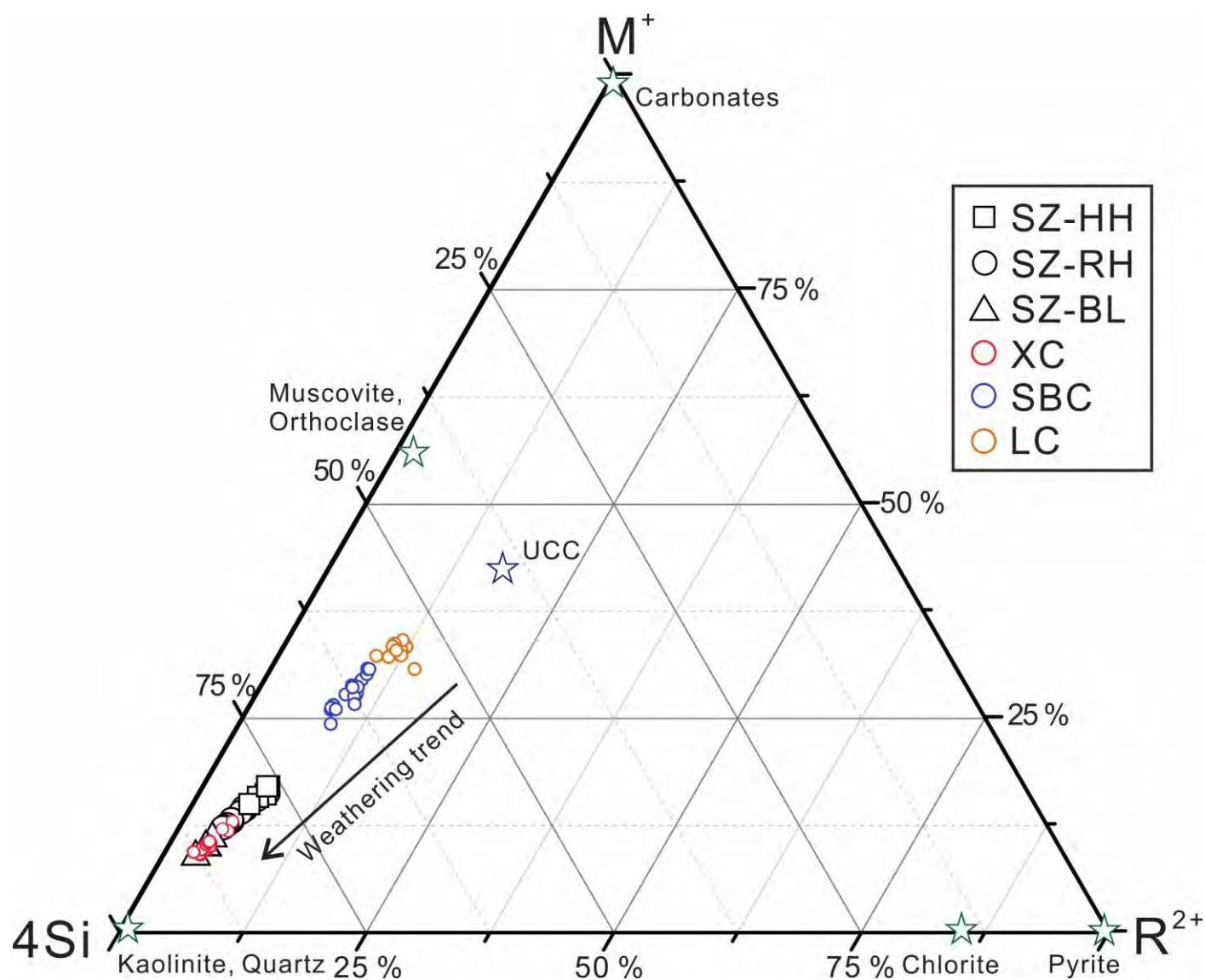
Figure 7. Chemical compositions of the Songzi and other soil sections in the diagram of the M^+-4Si-R^{2+} system. The panel shows that chemical weathering intensities generally increase in the following sequence: LC (Luochuan loess-paleosols from Chinese Loess Plateau, northern China; Chen et al., 2001) < SBC (Shangbaichuan loess-paleosols from eastern Qinling Mountains, central China; Fang et al., 2017) < Songzi = XC (Xuancheng red soil from Yangtze valley, southern China; Zhao et al., 2021).
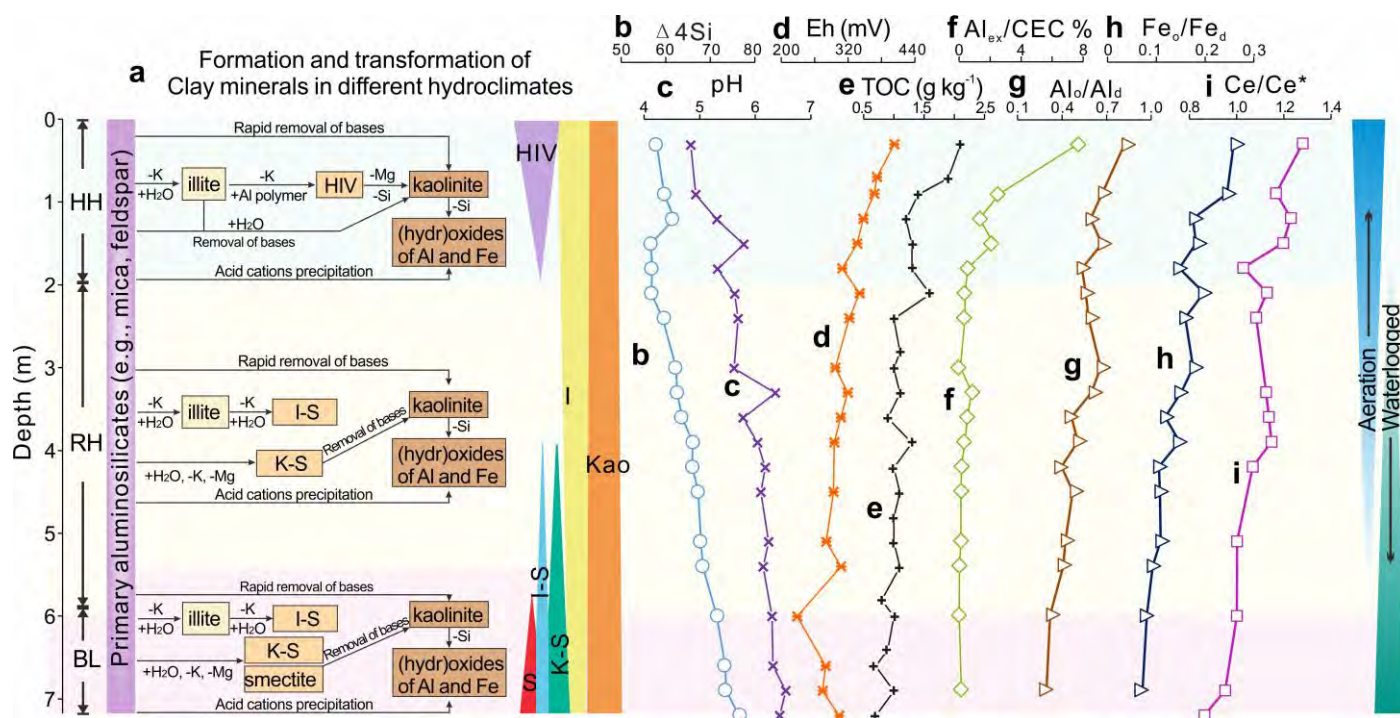
Figure 8. Variations in geochemical and physicochemical components in the Songzi section and clay-mineral alteration in different soil horizons. a) Possible clay evolution pathways at HH, RH, and BL. Depth profiles of b) weathering degree ($\Delta 4Si$), c) pH, d) Eh, e) TOC, f) Al_{ex}/CEC ratio, g) Al activity (Al_o/Al_d), h) Fe activity (Fe_o/Fe_d), and i) Ce anomaly (Ce/Ce^*) showing temporal hydroclimatic evolution at Songzi.
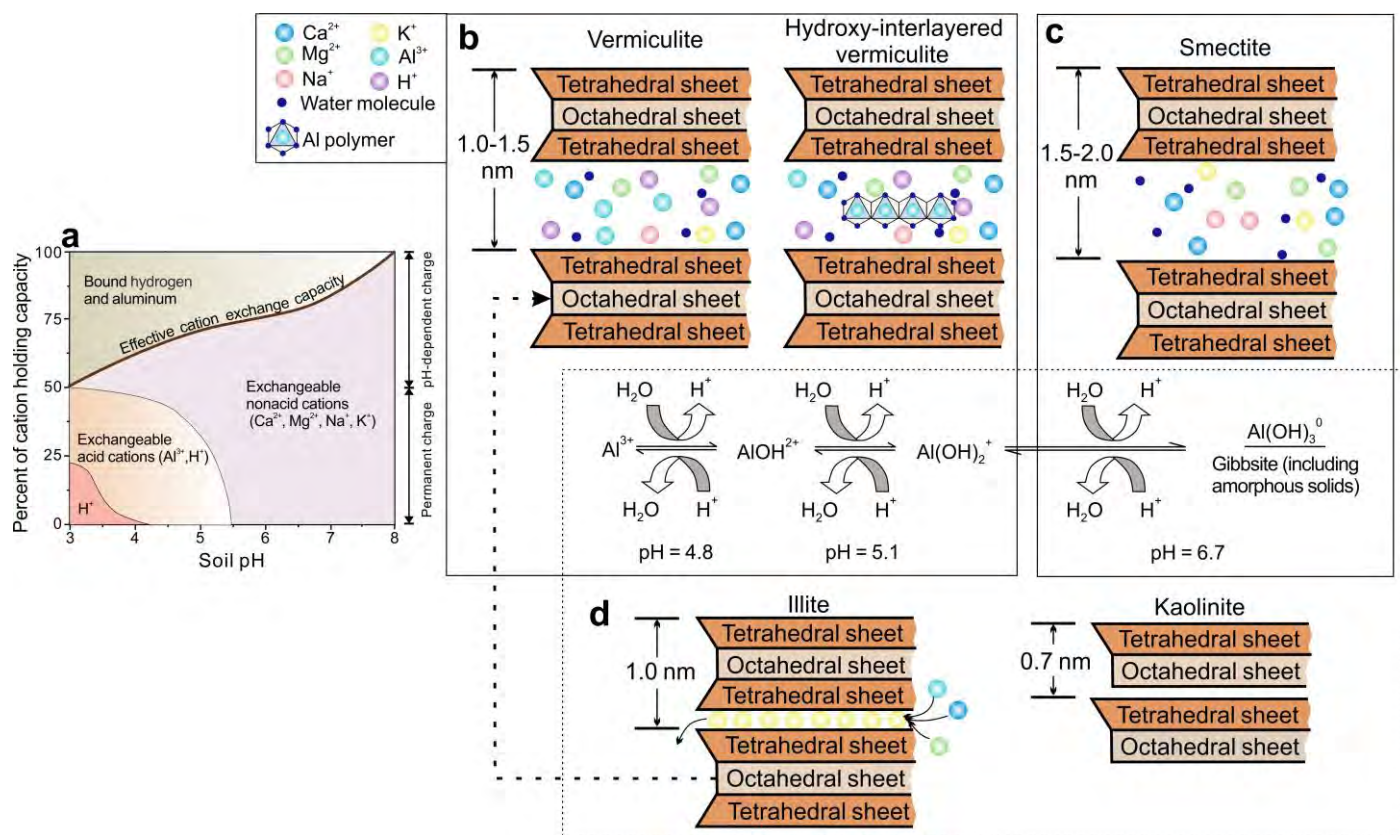
Figure 9. Schematic drawing illustrating the controls of soil acidic cation variations on clay-mineral transformation. a) General relationships between soil pH and the prevalence of various exchangeable and tightly bound cations in a mineral soil. At pH values above 5.5, the concentrations of exchangeable Al^{3+} and H^+ ions are negligible, and the effective CEC is completely saturated with exchangeable non-acid cations (Ca^{2+}, Mg^{2+}, Na^+, and K^+, the so-called 'base cations'). As pH decreases from 5.5 to 4.0, acid cations occupy an increasing portion of the remaining exchange sites. Exchangeable H^+ ions occupy a major portion of the exchange complex only at pH levels below 4.0 (modified from Weil and Brady, 2017). Optimal soil acidic pool conditions for occurrence of b) vermiculite group minerals, c) smectite group minerals, and d) kaolinite and illite.